

ARTICLE

Zn²⁺ decoration of microtubules arrests axonal transport and displaces tau, doublecortin, and MAP2C

Taylor F. Minckley¹, Lyndsie A. Salvagio¹, Dylan H. Fudge¹, Kristen Verhey³, Steven M. Markus², and Yan Qin¹

Intracellular Zn²⁺ concentrations increase via depolarization-mediated influx or intracellular release, but the immediate effects of Zn²⁺ signals on neuron function are not fully understood. By simultaneous recording of cytosolic Zn²⁺ and organelle motility, we find that elevated Zn²⁺ (IC₅₀ ≈ 5–10 nM) reduces both lysosomal and mitochondrial motility in primary rat hippocampal neurons and HeLa cells. Using live-cell confocal microscopy and in vitro single-molecule TIRF imaging, we reveal that Zn²⁺ inhibits activity of motor proteins (kinesin and dynein) without disrupting their microtubule binding. Instead, Zn²⁺ directly binds to microtubules and selectively promotes detachment of tau, DCX, and MAP2C, but not MAP1B, MAP4, MAP7, MAP9, or p150glued. Bioinformatic predictions and structural modeling show that the Zn²⁺ binding sites on microtubules partially overlap with the microtubule binding sites of tau, DCX, dynein, and kinesin. Our results reveal that intraneuronal Zn²⁺ regulates axonal transport and microtubule-based processes by interacting with microtubules.

Introduction

Free, labile zinc (referred to herein as Zn²⁺) has been suggested to act as an intraneuronal signaling molecule. Increases in cytoplasmic Zn²⁺ concentrations can occur as a result of influx from the extracellular milieu through several channels historically defined as Ca²⁺ channels (Hu et al., 2009). Alternatively, Zn²⁺ can be released from intracellular stores via the transient receptor potential mucolipin 1 (TRPML1) channel (Minckley et al., 2019; Du et al., 2021). Synchronous Zn²⁺ spikes have also been detected to fire along with neuronal excitation (Zhang et al., 2021). Such elevated Zn²⁺ has long-term transcriptional effects in neurons (Sanford et al., 2019; Wang et al., 2004). Bioinformatic studies have suggested that Zn²⁺ can bind 2,800 human proteins (Andreini et al., 2006), and in vitro studies have shown that physiological levels of Zn²⁺ inhibit certain enzymes (Eron et al., 2018; Hogstrand et al., 1999; Bellomo et al., 2014). However, it has yet to be determined whether changes in intraneuronal Zn²⁺ can rapidly elicit downstream effects at timescales comparable to Ca²⁺ signaling events. Moreover, if and how Zn²⁺ might directly affect neurophysiological processes is poorly understood.

Microtubule-based trafficking plays critical roles in neurons, which have axonal projections that can extend up to ~1 m in humans. The importance of proper axonal transport and

microtubule regulation is evident by the clear correlation between several neurodevelopmental and adult onset neurodegenerative diseases and mutations in several components of microtubule network and transport machinery (Morfini et al., 2009; Sleight et al., 2019; Markus et al., 2020; Lasser et al., 2018; Dubey et al., 2015). These processes are under precise spatiotemporal control for the establishment and maintenance of neuronal function and health. Microtubule-associated proteins (MAPs) are responsible for the stability and regulation of microtubule dynamics and microtubule-based function, including transport. Motor proteins comprise one subfamily of MAPs and include dynein and kinesin which are responsible for retrograde and anterograde trafficking along microtubules, respectively (Maday et al., 2014; Hirokawa et al., 2009). Recent work has established that various MAPs can influence polarized microtubule transport by either inhibiting or promoting motor protein motility along microtubules (Monroy et al., 2020). A subset of these motility- and stability-regulating MAPs are upregulated in neurons and are crucial for neuronal development and function. Together, motor proteins (and their cargo-binding adaptor proteins), MAPs, and the microtubules themselves provide numerous targets for regulation that help the cell to accomplish appropriate transport and microtubule regulation.

¹Department of Biological Sciences, University of Denver, Denver, CO, USA; ²Department of Biochemistry and Molecular Biology, Colorado State University, Fort Collins, CO, USA; ³Department of Cell and Developmental Biology, University of Michigan, Ann Arbor, MI, USA.

Correspondence to Yan Qin: yan.qin@du.edu.

© 2023 minckley et al. This article is distributed under the terms of an Attribution–Noncommercial–Share Alike–No Mirror Sites license for the first six months after the publication date (see <http://www.rupress.org/terms/>). After six months it is available under a Creative Commons License (Attribution–Noncommercial–Share Alike 4.0 International license, as described at <https://creativecommons.org/licenses/by-nc-sa/4.0/>).

In this manuscript, we uncover potent roles for Zn^{2+} in the regulation of microtubule-based processes. Neuron depolarization-induced Zn^{2+} influx arrested axonal transport of lysosomes, mitochondria, and DCVs, which was reversed upon Zn^{2+} chelation. Furthermore, physiological levels of Zn^{2+} directly inhibited motility of kinesin via a cargo-adaptor independent mechanism by interacting with microtubules. To determine the potential Zn^{2+} binding sites on microtubules, we investigated the effects of Zn^{2+} on microtubule-decoration of eight MAPs by confocal imaging. Our results show that increases in cytosolic Zn^{2+} induce fast and reversible dissociation of tau, DCX, and MAP2C from microtubules. We propose that Zn^{2+} , via direct interactions with microtubules, acts as a brake for axonal transport and redistributes DCX, MAP2C and tau in neurons.

Results

Zn^{2+} arrests axonal transport of lysosomes and mitochondria

Both Ca^{2+} and Zn^{2+} have been reported to inhibit mitochondrial motility in neurons (Yi et al., 2004; Wang and Schwarz, 2009; Malaiyandi et al., 2005). This led us to question whether this inhibition is limited to mitochondria, or if it could affect other organelles such as lysosomes. In order to determine the effects of Zn^{2+} on lysosomal trafficking, we used a live-cell time-lapse imaging experiment to monitor the movement of lysosomes along a section of an axon. A kymograph of the axon expressing LAMP1-mcherry was generated, and the active moving of lysosomes was indicated as diagonal lines in the kymograph (Fig. 1 A). The lysosomal speed was calculated by analysis of all lysosomal kymographs using the KymoButler (Jakobs et al., 2019) plug-in for Mathematica (Wolfram Research, Inc.). We increased intracellular Zn^{2+} concentrations in primary hippocampal neurons by triggering depolarization-induced extracellular Zn^{2+} influx (Sensi et al., 2009). Membrane depolarization with 50 mM KCl in the presence of 100 μM ZnCl_2 led to a significant decrease in the motility of both anterograde and retrograde lysosomes (Fig. 1, A–C and Video 1). Following Zn^{2+} influx, the percentage of moving lysosomes was reduced, and the proportions of stationary lysosomes were increased from 58.5 to 89.6% (Fig. 1, D and E). Upon treatment with 100 μM of the Zn^{2+} chelator TPEN (N,N,N',N'-tetrakis(2-pyridinylmethyl)-1,2-ethanediamine), motility immediately recovered to near-baseline levels. Although both retrograde and anterograde lysosomal motility (speed and proportion) were rescued to baseline levels upon addition of TPEN, anterograde motility was slower to recover. Conversely, neuron depolarization with 50 mM KCl and 2 mM CaCl_2 caused no significant reduction in lysosome motility, and rather, there was an increase in the velocity and proportion of anterograde-moving lysosomes (Fig. 1, F–I and Video 2).

We also observed that Zn^{2+} influx significantly decreased the motility of mitochondria marked by mito-mCherry (Fig. S1, A–E and Video 3), a phenomenon which has been previously reported (Malaiyandi et al., 2005). Upon TPEN addition, we observed a fast rescue of retrograde mitochondrial transport but a slower recovery of anterograde transport. In addition, the recovered motility with TPEN treatment could be completely

inhibited again by treating the cells with 100 μM ZnCl_2 and 2.5 μM pyrithione (a Zn^{2+} ionophore), indicating a highly reversible mechanism (Fig. S1, A–H).

Anterograde transport of lysosomes and mitochondria is primarily mediated by kinesin-1 (KIF5A, KIF5B, and KIF5C; Fan and Lai, 2022). In order to test whether the Zn^{2+} inhibition is only specific for kinesin-1-mediated cargoes, we also examined the effects of Zn^{2+} on the kinesin-3 (KIF1A)-mediated motility. Kinesin-3 is the primary motor for the anterograde transport of dense-core vesicles (DCVs), which can be labeled by neuropeptide-Y (NPY; Guedes-Dias et al., 2019) in hippocampal neurons. The axonal movement of DCVs marked by NPY-mCherry was slower than lysosomes (Fig. S1 I), consistent with previous reports (Nassal et al., 2022). Both anterograde and retrograde transports of DCVs were significantly inhibited by large Zn^{2+} influx induced with 20 μM ZnCl_2 and high KCl (Fig. S1, I–K). Addition of TPEN slowly recovered the movement of DCVs, indicating that the inhibition of Zn^{2+} on kinesin-3 mediated transport is also reversible. These results suggest that neuronal Zn^{2+} acts as a reversible brake on the axonal transport of lysosomes, mitochondria, and DCVs, implicating a universal role of Zn^{2+} , distinct from Ca^{2+} , in regulating microtubule-based trafficking.

Zn^{2+} inhibits organellar motility with a nanomolar IC_{50} in HeLa cells and neurons

We wondered whether Zn^{2+} could arrest microtubule-based trafficking in non-neuronal cell types and found that inhibition of organellar motility could also be seen in HeLa cells upon addition of 20 μM ZnCl_2 and 1.25 μM pyrithione (Fig. S2). As with neurons, organellar motility could be rescued with TPEN (Fig. S2 and Video 4). Copper can act as a competitor for certain Zn^{2+} binding sites on proteins (Foster et al., 2014), so we tested whether copper could induce the same inhibition of motility. Surprisingly, we found no inhibition of lysosomal motility in HeLa cells upon addition of 20 μM CuCl_2 and 2.5 μM pyrithione (Fig. S2 E). We then sought to determine the cytoplasmic concentration of Zn^{2+} that is necessary to inhibit motility. We simultaneously measured organellar motility and cytosolic Zn^{2+} concentrations by expressing either LAMP1-mCherry or mito-mCherry, and the genetically encoded Zn^{2+} sensor, GZn2P (Fudge et al., 2018) in HeLa cells (Fig. 2 A). GZn2P was chosen to measure the cytosolic Zn^{2+} concentrations because its binding affinity ($K_d = 352$ pM for Zn^{2+}) is compatible with the cytosolic Zn^{2+} concentration, while all commercially available small molecule Zn^{2+} sensors presented relatively lower binding affinity at nanomolar range and nonspecific subcellular localizations (Pratt et al., 2021). Zn^{2+} was chelated with TPEN to determine the minimum apo-state signal of GZn2P, followed by 100 μM ZnCl_2 to slowly increase cytosolic Zn^{2+} . Cells were then treated with 2.5 μM pyrithione to achieve maximal GZn2P signal (Fig. 2, B and C). Organellar motility was measured and plotted against the corresponding cellular Zn^{2+} concentrations (see Materials and methods), generating dose-response curves for Zn^{2+} -dependent inhibition of both lysosomes (Fig. 2, D and H, $\text{IC}_{50} = 7.01 \pm 2.08$ nM) and mitochondria (Fig. 2, E and H, $\text{IC}_{50} = 5.50 \pm 2.51$ nM). To confirm our HeLa cell findings, we

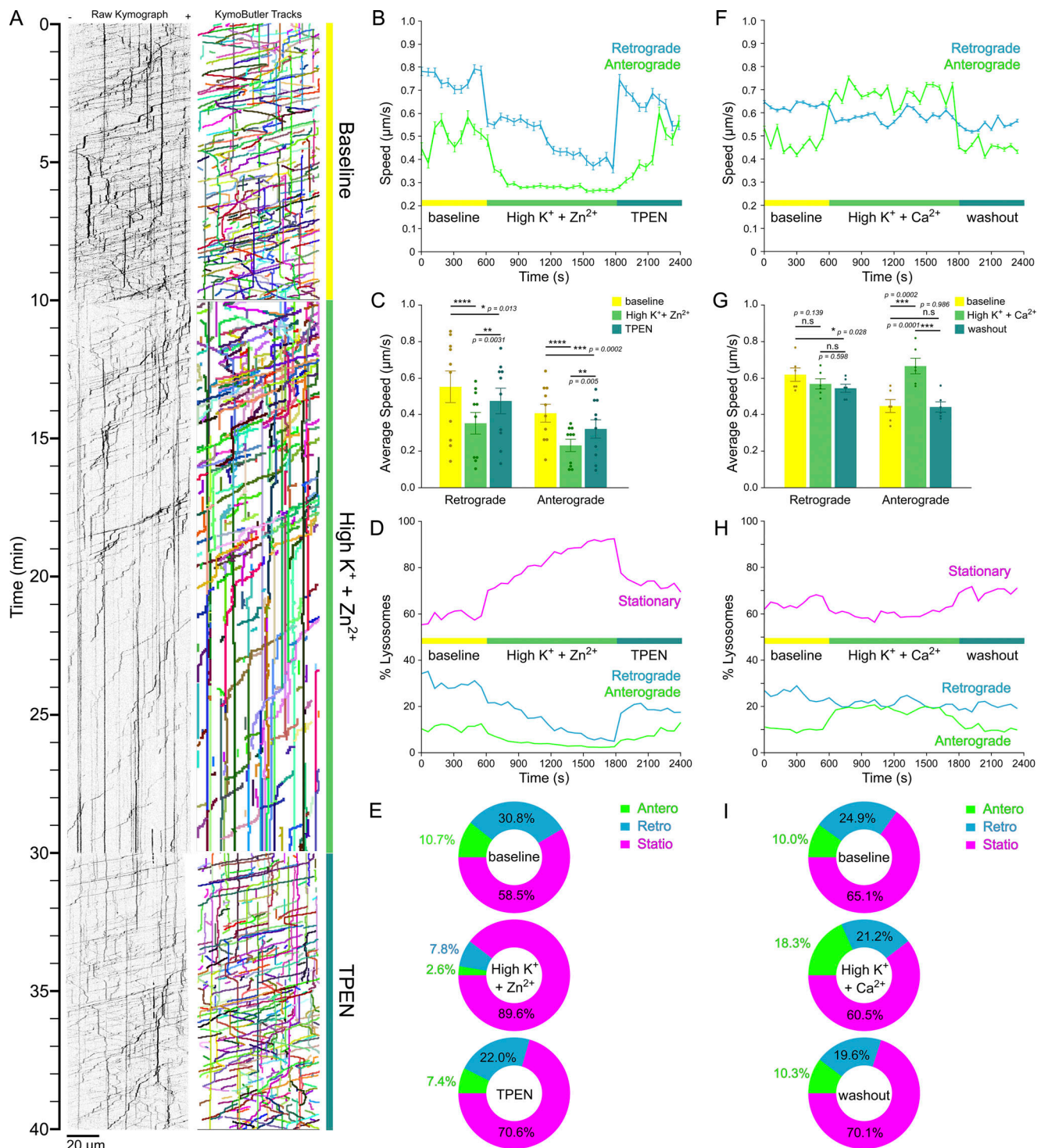


Figure 1. **Depolarization-induced influx of Zn^{2+} , not Ca^{2+} , arrests axonal transport of lysosomes.** (A) Representative kymographs (left) and measured tracks (identified using KymoButler; right) of LAMP1-mCherry motility along axons from primary cultured rat hippocampal neurons prior to ("baseline"; top) or after initiation of Zn^{2+} influx induced by 50 mM KCl depolarization (middle), and then following washout and addition of 100 μ M TPEN (bottom). (B) Mean instantaneous speed (\pm SEM) of lysosomes moving retrograde (blue) or anterograde (green) across baseline, Zn^{2+} influx by 50 mM KCl depolarization, and TPEN treatment (60-s binned, representing 10 axons). (C) Mean speed (\pm SEM) of lysosomes moving in the indicated directions for each condition ($n = 10$ axons from six independent replicates). Least-squares regression with post-hoc Tukey HSD. (D) Proportions of lysosomes moving in the indicated directions across baseline, depolarization, and TPEN treatment (60-s binned, representing 10 axons). (E) Mean proportions of lysosomal motility for each condition. (F) Mean instantaneous speed (\pm SEM) of lysosomes moving retrograde (blue) or anterograde (green) across baseline, 2 mM Ca^{2+} influx by 50 mM KCl depolarization, and washout (60-s binned, representing 10 axons). (G) Mean speed (\pm SEM) of lysosomes moving in the indicated directions for each condition ($n = 10$ axons from six independent replicates). Least-squares regression with post-hoc Tukey HSD. (H) Proportions of lysosomes moving in the indicated directions across baseline, 2 mM Ca^{2+} with 50 mM KCl, and washout (60-s binned, representing 10 axons). (I) Mean proportions of lysosomal motility for each condition. **** $P < 0.0001$, *** $P < 0.001$, ** $P < 0.01$, * $P < 0.05$, n.s. not significant.

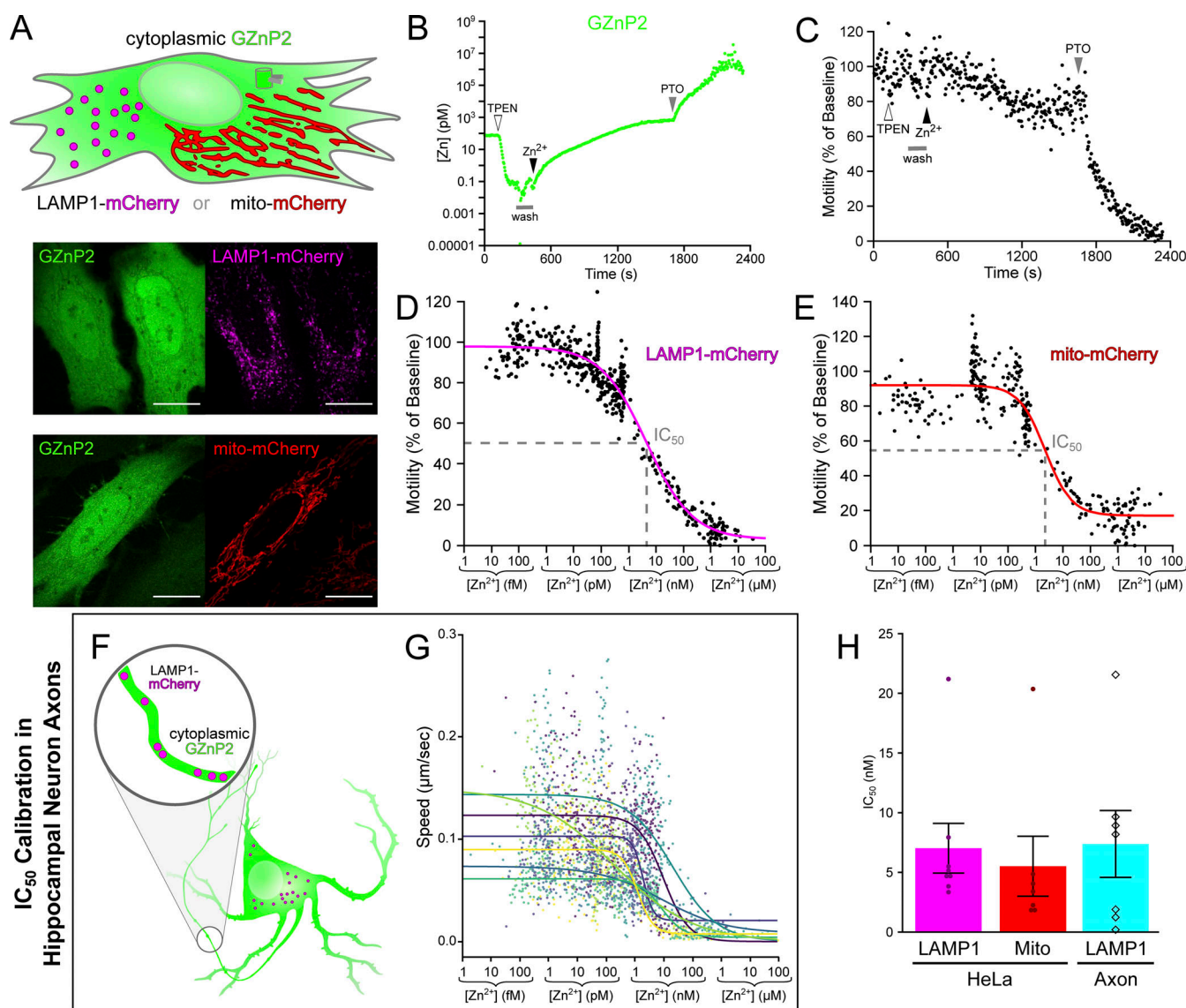


Figure 2. Zn^{2+} inhibits organellar motility with nanomolar IC_{50} in HeLa cells and neurons. (A) Schematic of the IC_{50} assay in HeLa cells (top) showing cytosolic localization of co-transfected GZnP2 sensor and either lysosomal (left, magenta) or mitochondrial (right, red) mCherry. Representative micrographs of HeLa cells (bottom) illustrating the localization of GZnP2 sensor in the cytoplasm and either LAMP1-mCherry (magenta, top) or mito-mCherry (red, bottom). Scale bar = 20 μm . (B and C) Representative plots of $[\text{Zn}^{2+}]$ (B; determined using GZnP2; see Materials and methods) and relative lysosomal motility (C; via LAMP1-mCherry) in a HeLa cell treated as indicated (100 μM TPEN at $t = 120$ s; a 2-min duration washout at $t = 300$ s; 100 μM ZnCl_2 at $t = 420$ s; and 5 μM pyrithione at $t = 1,680$ s). (D and E) Representative plot of relative motility versus $[\text{Zn}^{2+}]$ used to calculate IC_{50} values Zn^{2+} inhibition of (D) LAMP1-mCherry or (E) mito-mCherry motility. (F) Schematic of the IC_{50} assay in primary hippocampal neurons showing cytosolic localization of co-transfected GZnP2 sensor (green) and LAMP1-mCherry tagged lysosomes (magenta). (G) Overlaid plots of KymoButler-analyzed lysosome speed versus $[\text{Zn}^{2+}]$ used to calculate IC_{50} values for Zn^{2+} inhibition of lysosomes in neuron axons. The colors represent individual experiments in different axons. (H) Mean IC_{50} values ($\pm\text{SEM}$) for LAMP1-mCherry ("LAMP1") in HeLa cells (magenta; $n = 8$ cells from six individual replicates) or primary rat hippocampal neuron axons (cyan; $n = 7$ neuron axons from individual replicates) and mito-mCherry in HeLa cells ("Mito," red; $n = 7$ cells from five individual replicates). All experiments were performed in the absence of extracellular Ca^{2+} .

simultaneously measured axonal transport of lysosomes and axoplasmic Zn^{2+} concentration in primary hippocampal neurons and observed a strikingly similar threshold of Zn^{2+} inhibition (Fig. 2, F–H and Video 4, $\text{IC}_{50} = 7.38 \pm 2.80$ nM).

Zn^{2+} directly inhibits kinesin motility in a dose-dependent manner

Next, we investigated whether Zn^{2+} -mediated inhibition is a consequence of direct modulation of motor or cargo-adaptor

proteins by employing an inducible cargo trafficking assay. Constitutively active motors are recruited to transport vesicular cargoes in a cargo-adaptor-independent manner in living cells (Kapitein et al., 2010). A green fluorescent protein (mNeon-Green) and rapamycin binding fragment (FRB) are fused to the C-terminus of a constitutively active fragment of the neuron-specific kinesin-1 motor protein (KIF5A(1-560)-mNG-FRB; Hirokawa et al., 2009). Two FK506 binding proteins (2xFKBP) and a red fluorescent protein (mRFP) are fused to the

C-terminus of a peroxisomal membrane targeting sequence (PEX3(1-42)-mRFP-2xFKBP). When rapamycin or its analogs (i.e., Zotarolimus) are added to this system, FRB-FKBP heterodimerization is induced, and the motor protein and peroxisome are irreversibly tethered (Fig. 3 A), resulting in peroxisomes being transported from their generally static perinuclear position to the cell periphery (Schimert et al., 2019; Kapitein et al., 2010). With this system, we could directly assess KIF5A motility by measuring peroxisome movement and localization.

COS-7 cells were co-transfected with KIF5A(1-560)-mNG-FRB and PEX3-mRFP-2xFKBP (Schimert et al., 2019). Cytosolic KIF5A(1-560)-mNG-FRB fluorescent signal was visibly recruited to the peroxisomal membranes within seconds of Zotarolimus treatment (Fig. 3 C) and peroxisomes were rapidly dispersed to the periphery (Fig. 3 C and Video 5), measured by the average change in distance of peroxisomes from the geometric center of the cell (Fig. 3 B). Strikingly, when ZnCl_2 (2, 3, or 5 μM) was added along with pyrithione, peroxisome dispersion was dramatically reduced in a dose-dependent manner (Fig. 3, B and C; and Video 5). We quantified the inhibitory effect on peroxisomal distribution after 25 min of Zotarolimus treatment. Radial analysis of fluorescence intensity from the geometric cell center was conducted using a custom image processing macro written for ImageJ, and representative averages of all analyzed cells were generated (Fig. 3, D-F). Zotarolimus treatment led to a significant dispersion of peroxisomes compared with DMSO controls, which was almost entirely inhibited after Zn^{2+} influx (Fig. 3 G). Kinesin was still visibly recruited to peroxisomes in the presence of 5 μM Zn^{2+} (Fig. 3 C), indicating that Zn^{2+} does not interfere with FRB-FKBP heterodimerization.

Zn^{2+} does not cause motor proteins to detach from microtubules in situ and in vitro

Using oblique illumination microscopy, we observed that KIF5A(1-560)-mNG-FRB was highly enriched at the cell periphery and exhibited linear morphology, which colocalized with mCherry- α -tubulin signal, confirming that KIF5A interacts with and walks along microtubules toward their plus ends (Fig. 4 A). After 5 min treatment with 20 μM ZnCl_2 and 2.5 μM pyrithione, KIF5A(1-560) signal significantly shifted toward the center of the cell and away from the periphery (Fig. 4 A), quantified by the ratio of edge/center fluorescence intensity (Fig. 4 C). Pyrithione treatment alone had no effects on the distribution of KIF5A(1-560; Fig. 4, B and C). Confocal timelapse imaging also revealed redistribution of KIF5A(1-560), but no changes in the distribution or morphology of mCherry- α -tubulin (Fig. 4 D and Video 6), suggesting that Zn^{2+} influx blocked the movement of kinesin, but did not cause a massive microtubule catastrophe event. Importantly, Zn^{2+} did not cause dissociation of KIF5A from microtubules, as microtubule-localized KIF5A was still observed after Zn^{2+} treatment, most markedly near the center of the cell (Fig. 4 A). Further investigation showed that the microtubule association of KIF5A was unchanged after Zn^{2+} treatment as measured by “tubeness” analysis (Fig. 4, E and F).

The heavy-chain motor domain of human dynein (DHC1) is a significantly larger protein (4,646 amino acids) than kinesin and also requires multiple other components for processivity

(Kardon and Vale, 2009). Additionally, fluorescently tagged intermediate chains of this complex (i.e., IC2) must compete with endogenous proteins and result in a highly cytosolic fluorescent signal, and thus microtubule binding is difficult to discern (data not shown). Together, these obstacles make our in situ assays difficult to reproduce for dynein. Therefore, we measured motor protein binding to microtubules in vitro using total internal reflection fluorescence (TIRF) microscopy. We assessed the effect of Zn^{2+} on recombinant protein fragments that encompassed only the microtubule-binding domains (MTBDs) of yeast dynein and kinesin-1. In the case of dynein, this fragment (dyneinMTBD) is only 124 amino acids in length (compared to the full-length molecule, which spans 4,092 amino acids), and excludes all ATP-binding modules. To best ensure this fragment adopted a native fold that retains its microtubule binding activity, we fused dyneinMTBD to seryl tRNA synthetase (SRS) to create SRS-dyneinMTBD, as previously described (Ecklund et al., 2017; Carter et al., 2008; Gibbons et al., 2005; Fig. 4 G). For comparison, we also assessed a similar SRS-kinesinMTBD protein fusion (Fig. 4 G). Incubation with 100 μM ZnCl_2 did not cause a decrease in the motor MTBD fluorescence along coverslip-immobilized microtubules for both SRS-dyneinMTBD and SRS-kinesinMTBD (Fig. 4, H and I), which is in agreement with the in situ observation (Fig. 4, E and F). Therefore, Zn^{2+} directly modulates motor motility, but does not cause the motors to dissociate from microtubules.

Microtubule posttranslational modifications such as acetylation have been suggested to modulate axonal transport. For example, microtubule acetylation was reported to promote kinesin-1 mediated transport (Reed et al., 2006; Adalbert et al., 2020). We then investigated whether Zn^{2+} affects tubulin acetylation by immunostaining with antibody against acetylated α -tubulin and total endogenous β -tubulin. The results showed that there were no observed changes in acetylated α -tubulin along neuronal axons (Fig. S5, B-D), ruling out that tubulin acetylation is involved in the Zn^{2+} -mediated inhibition on motor motility.

Zn^{2+} directly binds microtubules and differentially modulates microtubule-stimulated ATPase activity of kinesin and dynein in vitro

Our live-cell imaging data clearly demonstrated that Zn^{2+} inhibits motor protein motility. Previous in vitro studies showed that millimolar concentrations of Zn^{2+} assembles purified tubulin into two-dimensional sheets and microtubules (Wolf et al., 1993) and micromolar Zn^{2+} inhibits the ATPase activity of kinesin (Böhm, 2017), though we observed in situ effects on motility in the nanomolar range. We therefore used accurately buffered Zn^{2+} solutions (from the picomolar to micromolar range) to examine the dose-dependent Zn^{2+} effects on microtubule-stimulated ATPase activity of both kinesin and dynein in vitro. We tested a commercially available human recombinant kinesin heavy chain (KIF5A, #KR01 Cytoskeleton) as well as an artificially dimerized, truncated yeast dynein motor domain fragment, which is sufficient for processive motility (Reck-Peterson et al., 2006) and exhibits high similarity to human dynein.

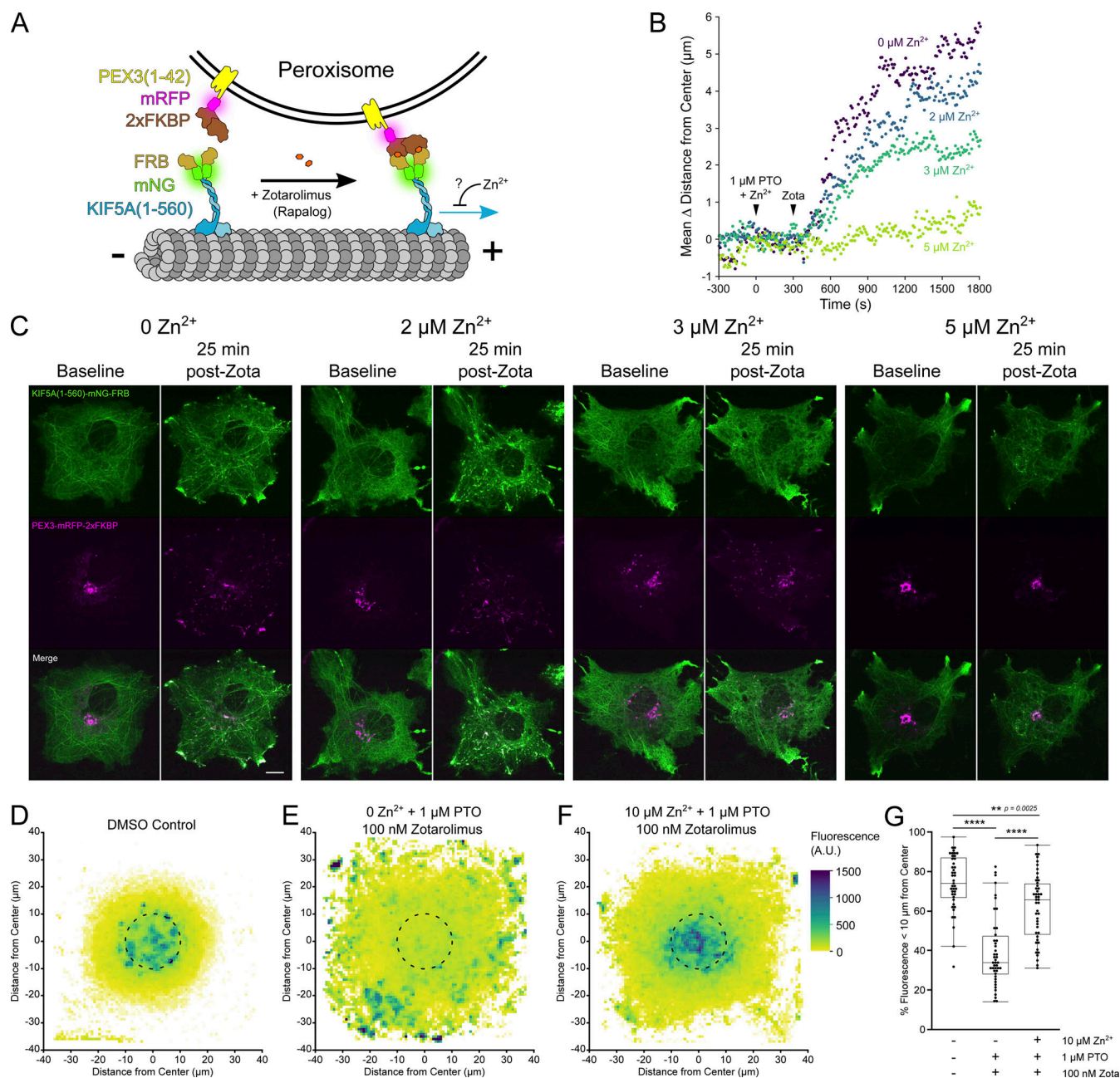


Figure 3. Zn^{2+} inhibits KIF5A movement in situ in a dose dependent manner. (A) Schematic of the components of the peroxisome dispersion assay. (B) Representative plots of mean change in peroxisome distance from the cell center over time, for COS-7 cells expressing KIF5A(1-560)-mNG-FRB and PEX3-mRFP-2xFKBP, treated at 0 s with 1 μM PTO and various concentrations of Zn^{2+} (none, purple; 2 μM , blue; 3 μM , teal; or 5 μM , lime), and 100 nM Zotarolimus ("Zota") at 300 s. (C) Representative micrographs of COS-7 cells expressing KIF5A(1-560)-mNG-FRB (green, top), PEX3-mRFP-2xFKBP (magenta, middle), or merged channels (bottom), at 0 s ("baseline") or 25 min after treatment with 100 nM Zotarolimus ("post-Zota") in the presence of the indicated Zn^{2+} concentrations. Scale bar = 10 μm . (D–F) Fluorescent intensity averages of PEX3-mRFP-2xFKBP in COS-7 cells co-expressing KIF5A(1-560)-mNG-FRB. Cells were imaged and aligned by their geometric centers after the following treatments and fixation: (D) 2 μl DMSO for 5 min, then an additional 2 μl DMSO for 25 min ($n = 42$ cells); (E) 1 μM PTO for 5 min, then 100 nM Zotarolimus for 25 min ($n = 44$ cells); (F) 10 μM ZnCl_2 and 1 μM PTO for 5 min, then 100 nM Zotarolimus for 25 min ($n = 46$ cells). Black dotted line indicates the area within 10 μm of the center. (G) Box plots and individual points representing the proportion of PEX3-mRFP-2xFKBP fluorescence within 10 μm of the geometric cell center, for the each of the conditions in (D–F). One-way ANOVA with post-hoc Tukey HSD. All experiments were performed in the absence of extracellular Ca^{2+} . **** $P < 0.0001$, ** $P < 0.01$.

We tested the microtubule-stimulated ATPase activity of these motors at varying Zn^{2+} concentrations using the EnzChek ATPase assay. Interestingly, we observed that KIF5A ATPase activity increases in response to picomolar levels of Zn^{2+} (peaking around 100 pM), but then is reduced as Zn^{2+} increases

into the nanomolar range (Fig. 5 A and Fig. S3 A). Alternatively, dynein activity is relatively stable across all picomolar Zn^{2+} concentrations and exhibits a similar decrease as Zn^{2+} increases into the nanomolar and micromolar range (Fig. 5 B and Fig. S3 B). Baseline ATPase activity (rate of ATPase per motor domain

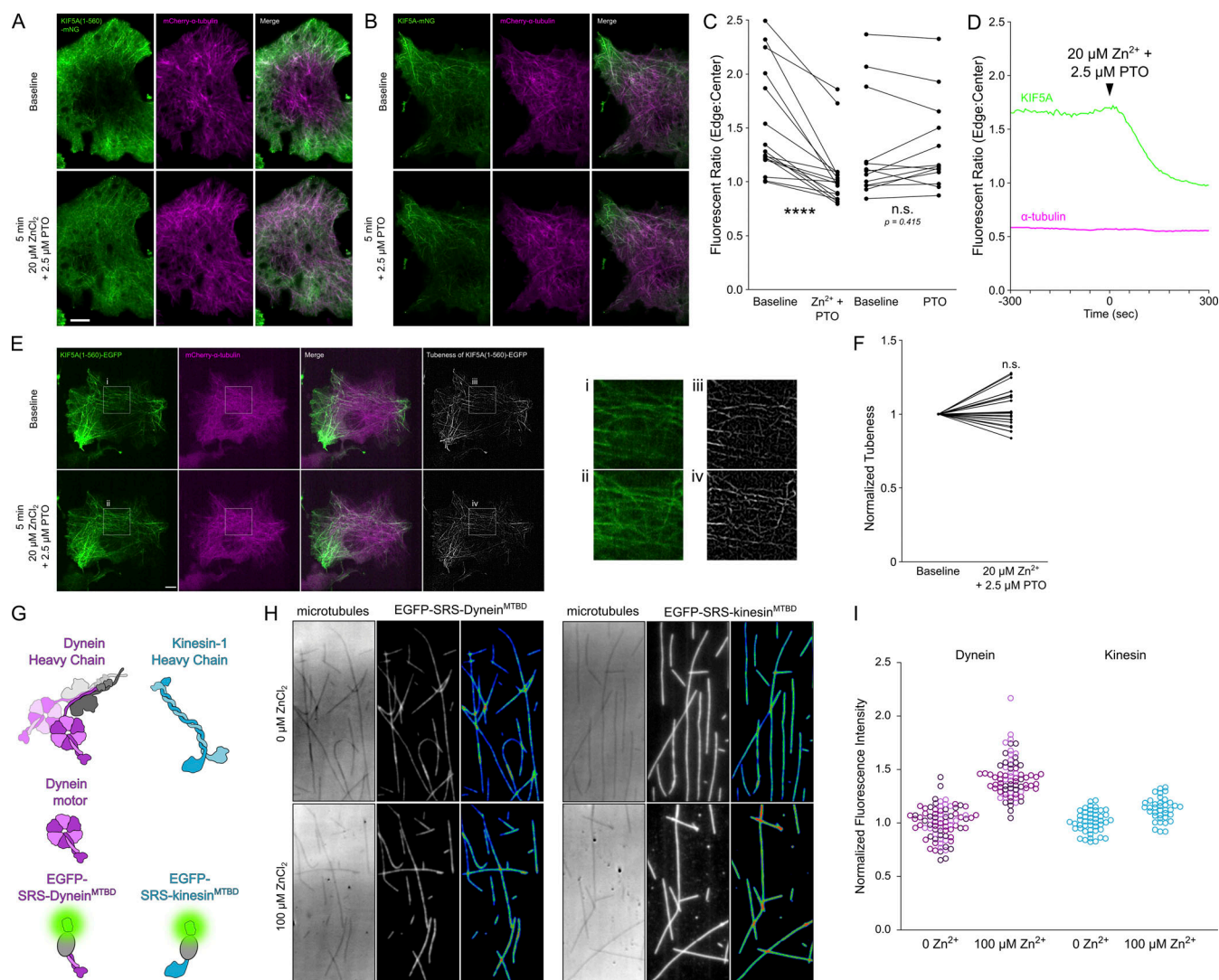


Figure 4. Zn^{2+} does not cause motor proteins to detach from microtubules in situ and in vitro. (A and B) Representative oblique illumination micrographs of COS-7 cells expressing KIF5A(1-560)-mNG-FRB (green, left) and mCherry- α -tubulin (magenta, middle), and merged channels (right). Cells were imaged at baseline (top) and 5 min after treatment (bottom) with (A) 20 μM ZnCl_2 and 2.5 μM pyriothione (PTO), or (B) 2.5 μM PTO alone. Scale bar = 10 μm . (C) Ratio of edge-to-center fluorescence of KIF5A(1-560)-mNG-FRB in COS-7 cells as treated in A and B (Zn^{2+} -treated, $n = 16$ cells from three individual biological replicates; PTO control, $n = 13$ cells from three individual biological replicates). Two-tailed paired t tests. (D) Representative timelapse plot of edge-to-center fluorescence ratio of KIF5A(1-560)-mNG-FRB (green) and mCherry- α -tubulin (magenta) in COS-7 cells, treated as in A. (E) Representative confocal micrographs of COS-7 cells expressing KIF5A(1-560)-EGFP (green, left) and mCherry- α -tubulin (magenta, middle left), merged channels (middle right), and "Tubeness" transformation (Fiji Plugin) of the KIF5A(1-560)-EGFP channel (right). Cells were imaged at baseline (top) and 5 min after treatment (bottom) with 20 μM ZnCl_2 and 2.5 μM PTO. Zoomed insets (i–iv, represented by white boxes) from the KIF5A(1-560)-EGFP and Tubeness transformation are shown at the far right. Scale bar = 10 μm . (F) Tubeness of KIF5A(1-560)-EGFP in COS-7 cells as treated in E, normalized to baseline ($n = 24$ cells from three individual biological replicates). Z test to ($x = 1$). All in situ experiments were performed in the absence of extracellular Ca^{2+} . (G) Cartoon representation of the dynein (left) and kinesin-1 (right) fragments used for in vitro binding assays. The full-length yeast dynein complex (left; heavy chain in purple with associated light, light-intermediate, and intermediate chains shown in gray) and full-length kinesin heavy chain and its associated fragments (right), and, along with the relevant fragments, are depicted. The SRS domain is represented as a gray oval, with EGFP shown in green. (H) Representative TIRF micrographs of coverslip-mounted taxol-stabilized microtubules (left, interference reflection micrographs), raw fluorescence of EGFP-labeled motor MTBDs (center), and pseudocolored fluorescence of motors MTBDs (right), for both dynein (left panels) and kinesin-1 (right panels), in the presence of either 0 ZnCl_2 (top) or 100 μM ZnCl_2 (bottom). (I) Dot plot of in vitro microtubule-localized fluorescent intensity (normalized to each replicate's respective average fluorescence) for the 0 Zn^{2+} control of EGFP-SRS-Dynein^{MTBD} (purple), EGFP-SRS-kinesin^{MTBD} (blue) in the presence of 0 Zn^{2+} ("Dynein," $n = 82$ microtubules, "kinesin," $n = 47$ microtubules) or 100 μM ZnCl_2 ("Dynein," $n = 74$ microtubules, "kinesin," $n = 37$ microtubules). Each dot represents a unique microtubule; each color indicates a separate replicate. **** $P < 0.0001$, n.s. not significant.

per second, "ATPase-motor⁻¹·sec⁻¹") for both kinesin (~2-5 ATPase-motor⁻¹·sec⁻¹) and dynein (~8-9 ATPase-motor⁻¹·sec⁻¹) is similar to the previously reported values (Fig. S3, A and B; Hancock and Howard, 1999; Huang et al., 2012;

Niekamp et al., 2019; Johnson, 1983). Finally, we observed that there was little to no reduction of ATPase activity of either kinesin or dynein in the presence of 500 μM Ca^{2+} (Fig. 5 C).

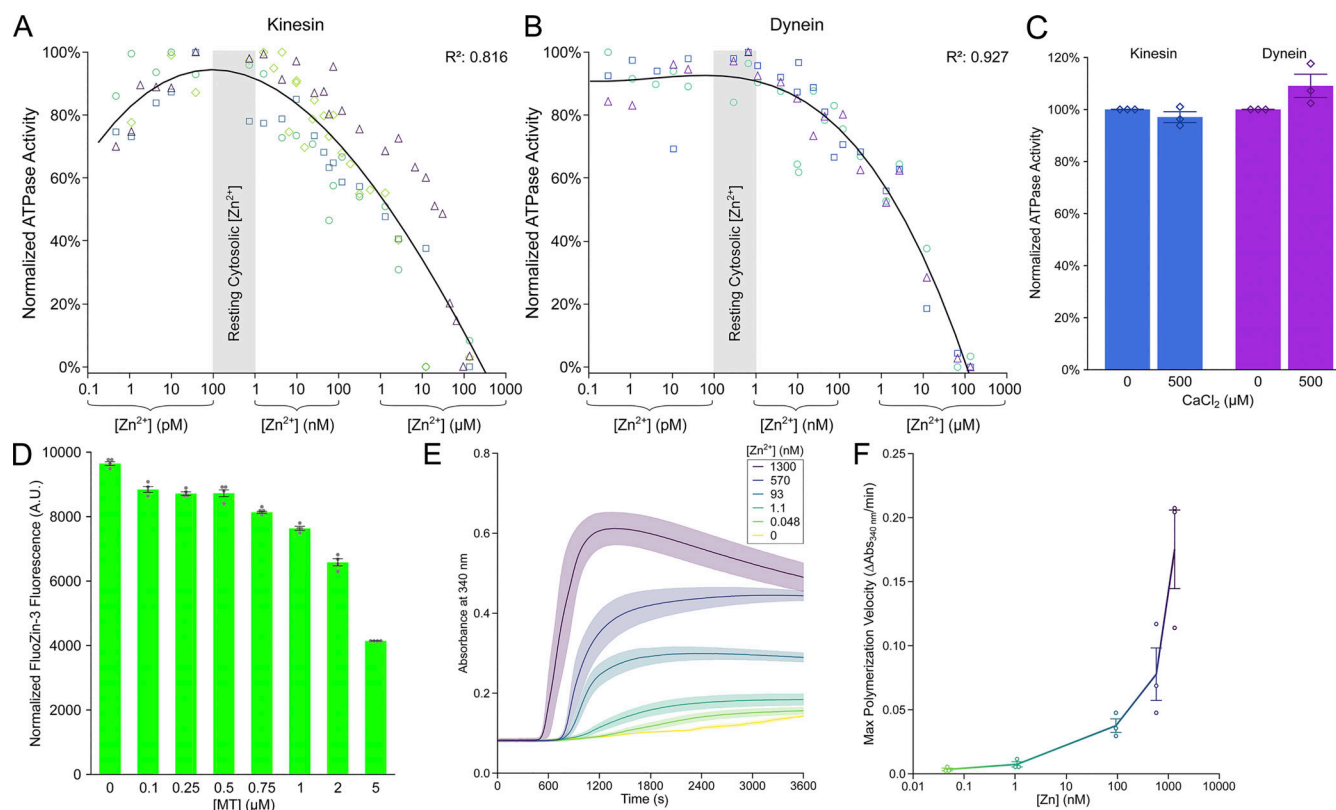


Figure 5. Zn²⁺ can bind microtubules and inhibits motor protein activity in vitro. (A and B) Microtubule-stimulated ATPase activity of (A) purified recombinant human kinesin (KIF5a), and (B) a minimally processive, artificially dimerized yeast dynein fragment (GST-dynein₃₃₁) across a range of precisely buffered Zn²⁺ concentrations (see Materials and methods), normalized to the maximum and minimum ATPase activity within each individual replicate, replicates denoted by separate colors and marker shapes (kinesin, *n* = 4 individual replicates; dynein, *n* = 3 individual replicates). Each assay was performed in the presence of 2 μM microtubules. Black line shows cumulative data fitted to cubic model with log transformation of [Zn²⁺] concentration, with corresponding R² values shown in the top right corner. (C) Mean normalized microtubule-stimulated ATPase activity (±SEM) for a minimally processive, artificially dimerized yeast dynein fragment (GST-dynein₃₃₁, purple) and recombinant human kinesin (KIF5A, blue) in the presence of 500 μM CaCl₂ (*n* = 3 replicates each). (D) Mean (±SEM) in vitro fluorescent intensity (488 nm excitation, 525 nm emission) for solutions containing 1 μM FluoZin-3, 1 μM ZnCl₂, 1 mM DTT, and varied concentrations of pre-formed, taxol-stabilized porcine microtubules (MT; *n* = 4 individual replicates). (E and F) Traditional turbidity assay of microtubule polymerization across a range of precisely buffered Zn²⁺ concentrations (see Materials and methods). (E) Mean absorbance (±SEM) at 340 nm and (F) maximum polymerization velocity for each Zn²⁺ concentration (*n* = 3 replicates per Zn²⁺ concentration). **** *P* < 0.0001, n.s. not significant.

Given that both kinesin and dynein ATPase activity can be inhibited by Zn²⁺ in vitro, we reasoned that Zn²⁺ might directly inhibit ATP hydrolysis or act on microtubules to inhibit motor protein motility. We then measured cellular ATP hydrolysis (ATP:ADP ratio) levels using the PercevalHR ATP sensor (Tantama et al., 2013) in COS-7 cells. The PercevalHR ratio was reduced when cells were treated with oligomycin that inhibits ATP synthase, confirming that the PercevalHR sensor was sensitive to changes in ATP hydrolysis (Fig. S3 C). Zn²⁺ influx was unable to alter intracellular ATP hydrolysis, (Fig. S3 C), indicating that the inhibition of Zn²⁺ on kinesin and dynein ATPase activity is not due to changes in available ATP in cells. Next, we explored whether Zn²⁺ can interact with microtubules. The small molecule Zn²⁺ sensor FluoZin-3 (*K_d* = 15 nM) was used to determine whether pre-polymerized canonical microtubules could chelate labile Zn²⁺ out of solution containing the sensor and Zn²⁺. As microtubule concentration increased, FluoZin-3 fluorescence intensity decreased (Fig. 5 D), indicating that microtubules can bind Zn²⁺. Furthermore, we sought to observe whether nanomolar concentrations of Zn²⁺ could influence

microtubule polymerization. Strikingly, Zn²⁺ increased the rate and extent of microtubule polymerization in a dose-dependent manner (Fig. 5, E and F). Together, these in vitro assays suggest that Zn²⁺ can directly bind to microtubules in cells and inhibit motor protein activity in the absence of other cellular components.

Zn²⁺ promotes the dissociation of tau, doublecortin, and MAP2C from microtubules in situ

To further understand the mechanisms by which Zn²⁺ inhibits the progression of motor proteins by interacting with microtubules, we tested if the microtubule-association of MAP proteins were affected by Zn²⁺. Recent work has highlighted that a range of MAPs can affect the microtubule-based trafficking of motor proteins (Monroy et al., 2018, 2020). We increased intracellular Zn²⁺ in COS-7 cells with 20 μM ZnCl₂ and 2.5 μM pyrithione and examined the microtubule decoration of eight different MAPs. For the five MAPs we examined, Zn²⁺ had no effects on the microtubule interaction of GFP-MAP1B, mEmerald-MAP4, EGFP-MAP7 (Fig. 6 A), EGFP-MAP9, or

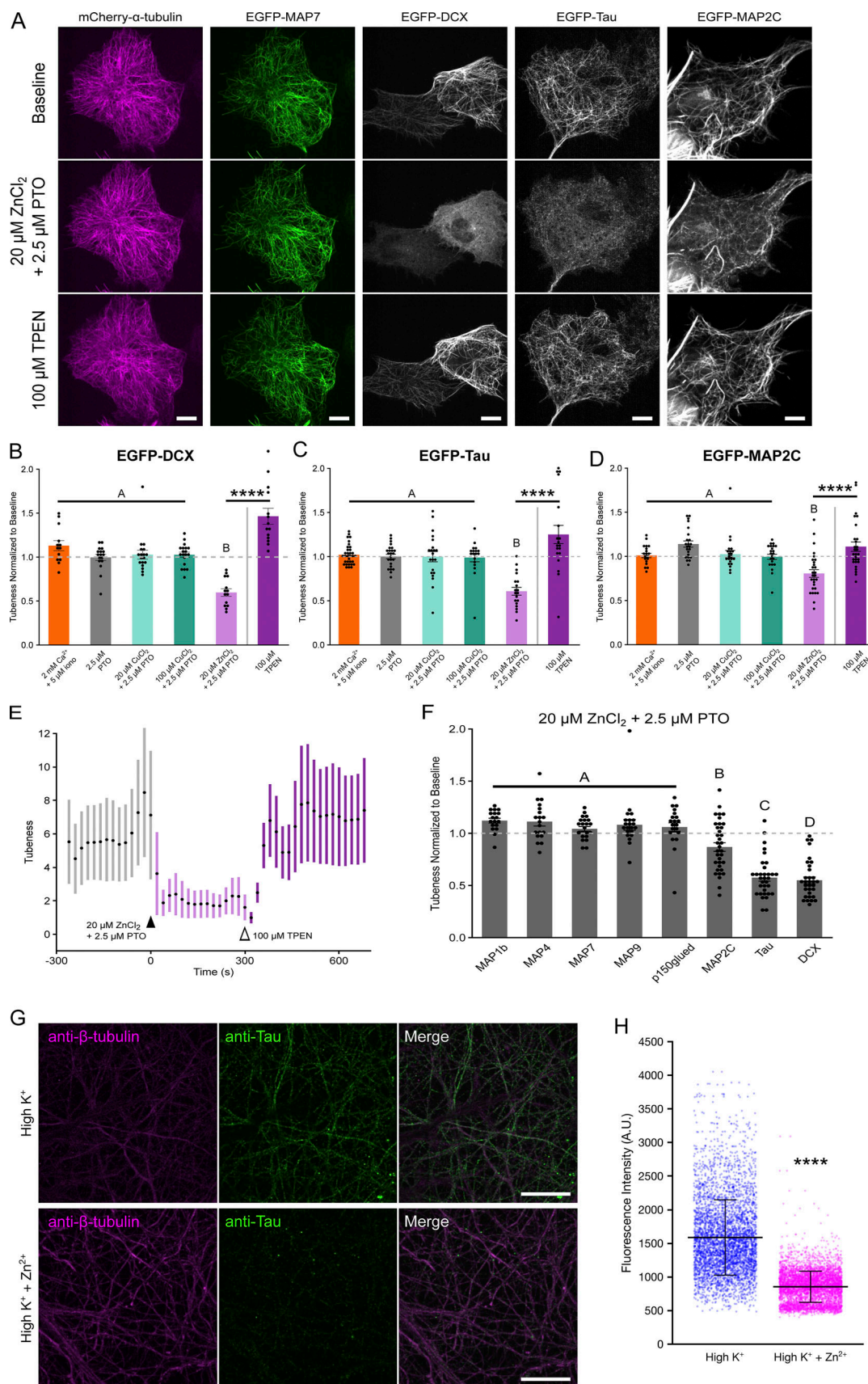


Figure 6. **Zn²⁺ promotes reversible detachment of DCX, tau, and MAP2C from microtubules in situ.** (A) Representative micrographs of COS-7 cells expressing mCherry-α-tubulin (magenta, left) and either EGFP-MAP7, EGFP-DCX, EGFP-Tau, or EGFP-MAP2C, before treatment ("baseline," top), after 5-min

treatment with 20 μM ZnCl_2 and 2.5 μM PTO (middle), or after subsequent treatment with 100 μM TPEN (bottom). Scale bar = 10 μm . **(B–D)** Mean tubeness ($\pm\text{SEM}$) of (B) EGFP-DCX, (C) EGFP-tau, or (D) EGFP-MAP2C normalized to baseline (gray dashed line), for the indicated treatments. Letters indicate statistically different groups (see Tables S1, S2, and S3). One-way ANOVA with post-hoc Tukey HSD. Zn^{2+} chelation rescue (100 μM TPEN) was measured with paired *t* test. **(E)** Representative time trace of microtubule morphology of EGFP-DCX in COS-7 cells as measured by “Tubeness” analysis (see Materials and methods and Fig. S4). Cells were treated with 20 μM ZnCl_2 at 0 s and 100 μM TPEN at 300 s. **(F)** Mean tubeness ($\pm\text{SEM}$) of the indicated microtubule-associated proteins in COS-7 cells treated with 20 μM ZnCl_2 and 2.5 μM PTO for 5 min, was normalized to baseline. Letters indicate statistically different groups (see Table S4). One-way ANOVA with post-hoc Tukey HSD. **(G)** Representative immunofluorescence micrographs of methanol-fixed primary rat hippocampal neurons depolarized with 50 mM KCl in the absence (top) or presence (bottom) of 100 μM ZnCl_2 . Fixed cells were incubated with anti- β -tubulin monoclonal antibodies (magenta, left), anti-tau polyclonal antibodies (green, center), and channels are shown merged (right). Scale bar = 10 μm . **(H)** Fluorescence intensity of AlexaFluor 488 secondary antibody-labeled tau decorating linear tubulin-positive regions across a 1 mm^2 area of neurons depolarized with 50 mM KCl in the absence (blue) or presence (magenta) of 100 μM ZnCl_2 (see Fig. S5 A for the stitched image of entire 1 mm^2 area; 50 mM KCl: $n = 4,330$ linear segments from two biological replicates; 50 mM KCl and 100 μM ZnCl_2 : $n = 4,820$ linear segments from two biological replicates). Unpaired *t* test assuming unequal variances. All experiments were performed in the absence of extracellular Ca^{2+} , except where indicated. **** $P < 0.0001$.

EGFP-p150glued as measured by “tubeness” analysis (Fig. 6 F). Strikingly, Zn^{2+} caused dissociation of EGFP-Tau, EGFP-DCX, and EGFP-MAP2C from microtubules within 5 min (Fig. 6, A–D and Video 7), without affecting microtubule morphology (Fig. 6 A and Fig. S4, A–C). In addition, microtubule association of EGFP-tau, EGFP-DCX, and EGFP-MAP2C could be rapidly rescued with Zn^{2+} chelation using 100 μM TPEN (Fig. 6, A–D and Video 7), suggesting a highly reversible mechanism as seen in the motility experiments. No decrease in microtubule association was seen with pyrithione treatment alone, nor with influx of Ca^{2+} (Fig. 6, B–D). In addition, we tested whether copper had similar effects, as tau has been shown to bind copper (Bacchella et al., 2020). Interestingly, 20 μM CuCl_2 and 2.5 μM pyrithione had no effects on EGFP-DCX or EGFP-MAP2C, and EGFP-tau (Fig. 6, B–D). We next examined if endogenous axonal tau was dissociated from microtubules by Zn^{2+} . Primary rat hippocampal neurons were treated for 5 min with 50 mM KCl with or without the presence of 100 μM ZnCl_2 , and immediately fixed with -20°C methanol to simultaneously permeabilize cells and preserve microtubule morphology (Gyparaki et al., 2021). Immunofluorescence with anti-tau antibodies showed clear decoration along axons in neurons treated with KCl alone, but Zn^{2+} caused a drastic reduction in axonal tau localization (Fig. 6, G and H; and Fig. S5 A).

The reversible regulation by Zn^{2+} on motility and microtubule-association of DCX, tau and MAP2C suggests that the striking effects are not a result of cell damage caused by Zn^{2+} influx. In addition, we showed that our Zn^{2+} influx conditions for COS-7 cells and neurons had no observable changes in nuclear morphology or chromatin compaction by Hoechst staining (Fig. S4, D and E), confirming that cells are viable and healthy through the imaging experiment.

An integrated atlas of microtubule-MAP interactions and predicted Zn^{2+} binding sites

Previous cryo-EM work has provided near-atomic models of microtubules (Manka and Moores, 2018) and their interaction with MAPs, including tau (Kellogg et al., 2018), DCX (Manka and Moores, 2020), kinesin (Shang et al., 2014), and dynein (Lacey et al., 2019). In order to simultaneously visualize where these MAPs bind on the microtubule lattice, we used the Protein-Ligand Interaction Profiler (PLIP; Salentin et al., 2015) to identify the amino acid residues on α - and β -tubulin which directly interacted with each of these MAPs (Fig. 7 A). All these MAPs

bind in unique areas along the microtubule surface, with most binding along the “ridge” of the protofilaments. Though these MAPs interacted with microtubules in distinct areas, all four MAPs had some interaction with helix-12 (Uchimura et al., 2010) of α -tubulin. We wondered whether there are overlapping sites among these four MAPs and Zn^{2+} that can account for the Zn^{2+} -induced dissociation of tau and DCX and inhibition of motor protein motility. In order to explore this, we performed bioinformatic analysis on the 3D protein structure of microtubules using the MIB Server (Lin et al., 2016), and rendered the 3D model of microtubules to visualize these binding sites (Fig. 7 B). Surprisingly, there were a number of domains on the outer surface of the microtubule with high prediction scores for Zn^{2+} binding on α -tubulin, specifically on helix-12 (Fig. 7, B and C). There was a significant overlap between the predicted Zn^{2+} binding sites and the MAP-interacting residues, as well as residues within 5 Å of these sites, specifically on α -tubulin as compared to β -tubulin (Fig. 7, C and D). We identified a cluster of residues with both high Zn^{2+} binding scores and significant MAP interactions, including H192, E196, E417, E420, E423, and D424. One site involving H192, E420, and D424 is particularly favorable for Zn^{2+} binding to form a tetrahedral geometry within 2–3 Å distance to a Zn^{2+} ion (Fig. 7 Bii). One water molecule or E196, which directly interacts with DCX (Fig. 7 Ai) and is only 5.3 Å from this Zn^{2+} site, may act as the fourth Zn^{2+} coordination site. Tau has been found to sterically hinder motor protein binding to microtubules (Dixit et al., 2008). Given the location of Zn^{2+} binding sites on microtubule surface, Zn^{2+} could compete with MAPs for the same amino acid binding sites, or induce a conformational change in these MAP-binding regions of microtubules. This could cause the dissociation of tau and DCX and blocking of motor protein progression.

Discussion

Long-distance axonal transport requires coordinated and precise regulation to ensure delivery of appropriate cargo to its requisite destination. Our results reveal that Ca^{2+} does not inhibit lysosomal motility, but Zn^{2+} can inhibit axonal transport of mitochondria, lysosomes, and DCVs (Fig. 1 and Fig. S1). Such inhibition was detected when Zn^{2+} concentration was increased to low nanomolar range ($\text{IC}_{50} = 5\text{--}10$ nM, Fig. 2), which is within the range of previous estimates of the physiological fluctuations in cytosolic Zn^{2+} concentration (Maret, 2017). We further clarify

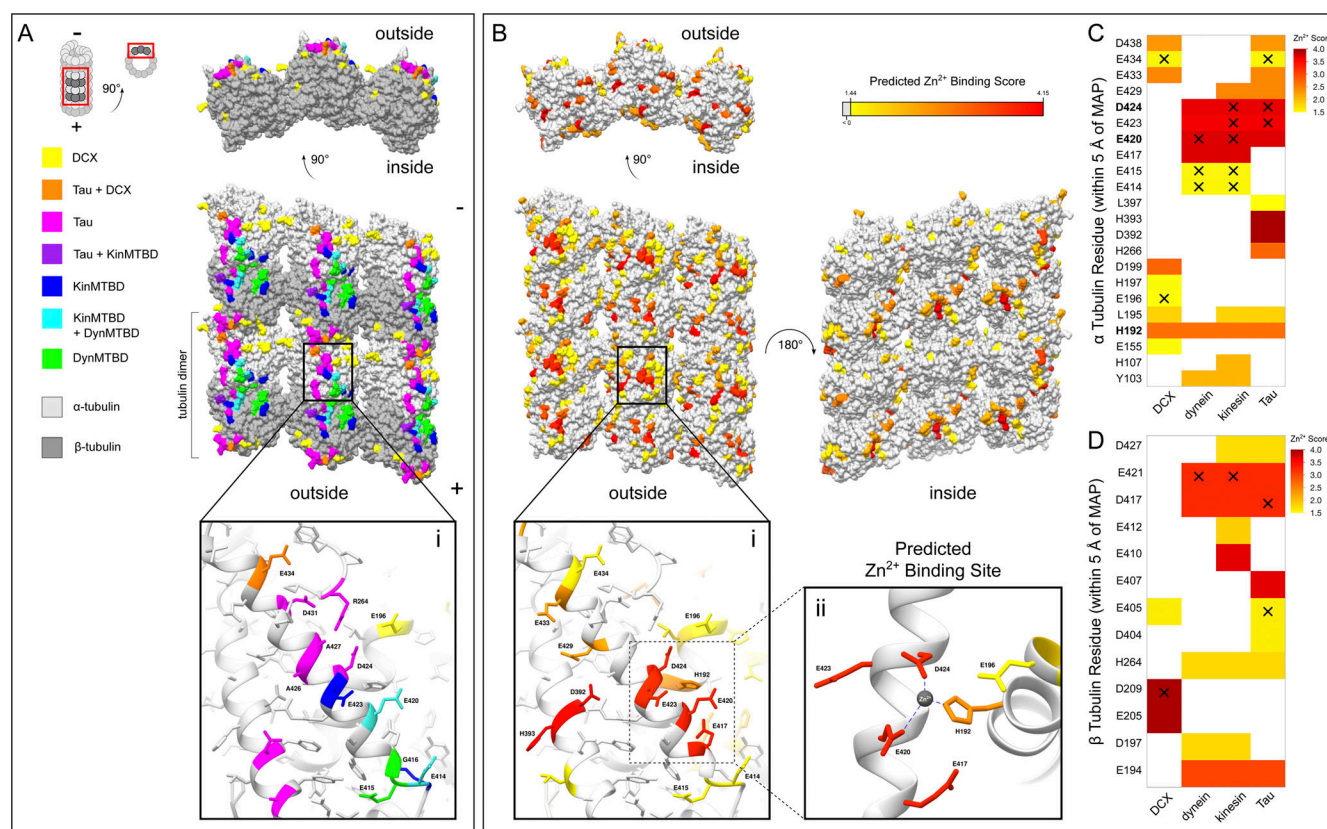


Figure 7. **Analysis of cryoEM-resolved MAP and predicted Zn²⁺ binding sites on microtubules.** (A and B) 3D protein model of cryo-EM microtubule reconstructions (PDB ID: 6EVY), with 6 tubulin dimers shown across three protofilaments (red boxes from inset schematic). (A) Amino acids of α -tubulin (light gray) and β -tubulin (dark gray) are color-coded to represent which MAPs directly interact at that residue as calculated by the Protein-Ligand Interaction Profiler (PLIP) from cryo-EM reconstruction models for DCX (PDB ID: 6REV), tau (PDB ID: 6CVN), kinesin microtubule binding domain ("KinMTBD," PDB ID: 3J8X), and dynein microtubule binding domain ("DynMTBD," PDB ID: 6RZB). (B) Tubulin amino acids are color coded to represent predicted Zn²⁺-binding sites (red = high score, yellow = moderate score, light gray = low score) as calculated by the MIB Server (see Materials and methods) (Lin et al., 2016). Insets (i) in each black box show the amino acids on or near helix 12 of α -tubulin that interact directly with the color-coded MAPs (A) or that are predicted Zn²⁺ binding residues (B). (ii) Predicted Zn²⁺ binding site between H192, E420, and D424. Dotted lines represent 2–3 Å distances between the predicted Zn²⁺ binding residues and the Zn²⁺ ion (gray). (C and D) Zn²⁺-binding prediction scores of α -tubulin (C) and β -tubulin (D) amino acid residues within 5 Å of the residues that interact with the indicated MAPs. "X" indicates residues that directly interact with the specified MAP. Bolded residue names for amino acids that are shown in (Bii).

that Zn²⁺-dependent inhibition of organelles is due to a direct block of motor protein progression (Fig. 3). Further, in situ confocal and in vitro TIRF imaging demonstrates that Zn²⁺ does not cause the dissociation of motor proteins from microtubules (Fig. 4). Our in vitro work also suggests that Zn²⁺ ions directly bind to sites along microtubules (Fig. 5, D–F and Fig. 7). We demonstrate that Zn²⁺ is able to reduce the ATPase activity of both kinesin and dynein in vitro (Fig. 5, A and B), but with higher inhibitory concentration than that of in situ (high nanomolar vs. low nanomolar). Such discrepancy suggests that Zn²⁺-mediated inhibition might be due to a conformational change on microtubules, which may require higher Zn²⁺ concentrations in artificially stabilized microtubules used in vitro than the endogenous microtubules in cells. Our results further support the direct microtubule-binding hypothesis as elevated levels of Zn²⁺ can selectively detach tau, DCX, and MAP2C, not the other five MAPs, from microtubules (Fig. 6). We also show that even short-term (5 min) elevations in Zn²⁺ drastically reduce endogenous binding of tau to microtubules in hippocampal neurons (Fig. 6, I and J). Finally, the predicted Zn²⁺ binding sites

on microtubules sit at the intersection of published, cryoEM-resolved microtubule binding sites of tau, DCX, dynein, and kinesin (Fig. 7), indicating that Zn²⁺ binding exhibits allosteric effects on the interaction between MAPs and microtubules.

Zn²⁺ decoration of microtubules as a microtubule-based mechanism for motility and MAP regulation

Microtubules not only act as long tracks for motor protein-based transport, but also govern the direction and motility of transport through binding of MAPs or post-translational modifications. Previous studies have demonstrated that differential decoration of microtubules with various MAPs can affect the recruitment and processivity of both kinesin and dynein. Specifically, tau and DCX can mediate greater inhibitions on kinesin-1 motility than on dynein motility, likely due to the steric hindrance of the larger kinesin MTBD as compared to the dynein MTBD (Vershinin et al., 2008; Tan et al., 2019; Chaudhary et al., 2018; Monroy et al., 2018; Monroy et al., 2020). Kinesin-1 motility is robustly inhibited by MAP2C (Monroy et al., 2020), though there is limited direct single-molecule research on the interaction of

MAP2C and dynein. Kinesin-1 motility is also inhibited by other MAPs (DCLK1 and MAP9) but is increased by MAP7 (Monroy et al., 2020), while MAP7 does not affect dynein motility (Monroy et al., 2018). Interestingly, our results showed that the inhibitory effects of Zn^{2+} influx were stronger and faster on anterograde transport than retrograde transport (Fig. 1 B and Fig. S1 B), suggesting that Zn^{2+} might also mediate more potent inhibition on kinesin-1 than dynein.

Post-translational modification of microtubules (including acetylation, (poly)glutamylation, (poly)glycylation, and detyrosination) may affect both the binding of MAPs, as well as motor protein function (Janke and Bulinski, 2011; Janke and Magiera, 2020). Microtubule acetylation has been shown to increase axonal transport by directly increasing recruitment of kinesin motors (Reed et al., 2006), and alpha tubulin acetyltransferase 1 (ATAT1) and histone deacetylase 6 (HDAC-6) have been shown to control the acetylation status of microtubules (Even et al., 2019; Zhang et al., 2003). Further, excessive polyglutamylation has been shown to reduce axonal transport (Magiera et al., 2018), and this tubulin modification is controlled in part by TTL family tubulin polyglutamylase complex subunit L1 (TTLL1) and cytosolic carboxypeptidase 1 (CCP1; Bodakuntla et al., 2021; Rogowski et al., 2010). Interestingly, deglutamylases and deacetylases specifically have been long known to be Zn^{2+} -dependent metalloproteins (Porter and Christianson, 2019; Rogowski et al., 2010), though the second-to-minute effects of transient Zn^{2+} dynamics on these enzymes in cells had not been explored. Here we showed that increases in cellular Zn^{2+} had no effects on microtubule acetylation (Fig. S5, B–D). The Zn^{2+} -mediated effects on axonal transport and MAPs association with microtubules are relatively rapid (within minutes) and highly reversible with TPEN treatment, while the post-translational modifications are only preferred for a subset of microtubules (Montagnac et al., 2013), suggesting that enzyme-mediated covalent modifications might not be involved in the observed regulations by Zn^{2+} .

In this work, we demonstrate a conceptual advance in the field by revealing that decoration of microtubules with Zn^{2+} can also regulate organellar motility. This mechanism is distinct from Ca^{2+} -mediated regulation, which is mitochondria-specific and cargo adaptor-dependent. The inhibitory effect of Ca^{2+} on mitochondrial motility has been demonstrated in many cell types (neurons, HeLa, and H9c2 myoblasts; Yi et al., 2004), and the underlying molecular mechanisms have been well established. Increased Ca^{2+} signals can be sensed by the cytosolic EF-hand domains of the Miro protein, a transmembrane protein localized on the outer-mitochondrial membrane (Fransson et al., 2006). Ca^{2+} binding to Miro promotes binding to the heavy chain of kinesin, outcompeting kinesin binding to microtubules, and therefore arresting microtubule-based mitochondrial motility (Wang and Schwarz, 2009). In contrast, we demonstrated that Zn^{2+} can non-selectively inhibit organellar motility (of lysosomes, mitochondria, and DCVs), and further identified that Zn^{2+} -dependent transport inhibition works via a cargo-independent, but microtubule-dependent, mechanism.

Our data present a stronger argument for a direct effect of Zn^{2+} on microtubules. First, both the in situ inducible

peroxisome dispersion assay and in vitro motor protein ATPase assay reveal that Zn^{2+} can directly block motor protein movement in the absence of cargo-motor adaptors, MAPs, and post-translational modification enzymes. Second, the Zn^{2+} effects we observe either on organellar motility or MAP detachment are highly and rapidly reversible, demonstrating a more direct interaction between Zn^{2+} and microtubules. Third, the in vitro binding and polymerization assays reveal that Zn^{2+} can directly bind microtubules. Previous in vitro studies also supported that there are Zn^{2+} binding sites on tubulin (Wolf et al., 1993; Craddock et al., 2012). Our findings that Zn^{2+} only displaces tau, DCX, and MAP2C (but not MAP9 or MAP7) narrow down the Zn^{2+} binding sites on microtubule surface. The H192, E420, and D424 residues on microtubule surface form a Zn^{2+} binding pocket, which overlaps with the binding sites for tau/MAP2 and DCX. Zn^{2+} can compete with tau/MAP2 and DCX for the binding sites on microtubules but may also inhibit motor movement via a similar mechanism as tau/MAP2 by inducing a conformational change in the microtubule. However, it is still possible that Zn^{2+} may have indirect effects on microtubule post-translational modification that could possibly contribute to altered motor movement. Though beyond the scope of the data presented here, this is an enticing avenue for future research.

Physiological significance of Zn^{2+} -dependent motility and MAP regulation

As neurons rely on the well-coordinated transport of various axonal cargoes with a high degree of spatial and temporal precision, our findings provide an important new role for Zn^{2+} and the consequences of its imbalance in the development and progression of neuronal disease. Neurons have relatively high Zn^{2+} concentration (Sensi et al., 2009), as well as unique Zn^{2+} -handling mechanisms, resulting in neuron-specific storage of Zn^{2+} in endolysosomes and synaptic vesicles (Palmiter et al., 1996; Minckley et al., 2019) and unique cytosolic Zn^{2+} buffering (Howells et al., 2010). As compared to other cell types, neurons also have highly dynamic cytosolic Zn^{2+} signals (Minckley et al., 2019; Zhang et al., 2021). Our work reveals a new regulation mechanism of microtubule-based processes and highlights Zn^{2+} as an ionic signal for proper neurodevelopment and neuronal function. Local increases in cytosolic Zn^{2+} can result from influx through VGCCs in the soma or axon terminals (Sensi et al., 2009; Sanford and Palmer, 2020; Zysk et al., 2018) or NMDA-dependent Zn^{2+} influx at synapses (Nakashima and Dyck, 2009; Sensi et al., 2009). Neurons can also release their lysosomal pools of Zn^{2+} through the lysosomal ion channel, TRPML1 (Minckley et al., 2019). These local Zn^{2+} signals may cause organelles to stop or pause in order to deliver their cargo, such as Shank proteins, to the postsynaptic regions during synaptogenesis and synapse maturation (Grabrucker et al., 2011). Mitochondria are tethered to axonal microtubules by syntrophin to provide local energy metabolism important for synapse function (Kang et al., 2008), and proper Zn^{2+} homeostasis may be important for maintaining proper mitochondrial distribution and subsequent synaptic energy supply. Additionally, we observed different responses of dynein and kinesin to low concentrations of Zn^{2+} , and changes in local Zn^{2+}

concentration may potentially favor either anterograde or retrograde trafficking events. This could play an important role in the balance of motor protein “tug-of-war” for cargoes which are decorated with both kinesin and dynein. Long-term changes in Zn^{2+} concentrations may also signal a cell-wide change in motility, wherein motility in the anterograde (i.e., high picomolar to low nanomolar Zn^{2+}), retrograde (i.e., low picomolar Zn^{2+}), or neither (i.e., >10 nM Zn^{2+}) direction is favored. Slight changes in cytosolic Zn^{2+} concentration could result in the perturbation of the fine-tuned regulation of axonal cargo transport between the soma and axonal growth cones or synaptic terminals.

The Zn^{2+} -dependent detachment of MAPs occurs within seconds of Zn^{2+} influx and is completely reversible within seconds of Zn^{2+} chelation. This highlights the importance of Zn^{2+} homeostasis on second-to-minute timescales, as changes in Zn^{2+} concentration can acutely modulate microtubule-based processes, including motor protein function and MAP decoration. Local or global elevation of Zn^{2+} may therefore lead to spatio-temporal control of DCX in growing neurites, as well as proper redistribution of tau and MAP2C to axons and dendrites, respectively. All these Zn^{2+} -regulated MAPs have established roles in neuronal development and morphological determination of axons and dendrites (Fu et al., 2013; Kosik and Finch, 1987). For Zn^{2+} -insensitive MAPs, MAP1B is vital for neuronal migration, guidance, and elongation of neuronal axons during development (Meixner et al., 2000; Yang et al., 2012), while MAP7 has been shown to be crucial for neurite branching (Tymanskyj et al., 2017, 2018). The distinct roles of Zn^{2+} -sensitive MAPs (tau, DCX, and MAP2C) and Zn^{2+} -insensitive MAPs (MAP1B and MAP7) suggest that Zn^{2+} signals can influence certain neuronal function by selectively regulating a subset of MAPs. Our findings open the door for future research to determine the exact MAP code in neuronal axons that may be favored by various concentrations of Zn^{2+} .

Pathological significance of Zn^{2+} -dependent motility and MAP regulation

It is known that defects in axonal transport can lead to several adult onset neurodegenerative diseases, including Alzheimer’s disease, Huntington’s disease, amyotrophic lateral sclerosis (ALS), spinal muscular atrophy with lower extremity dominance (SMA-LED), and Parkinson’s disease (Morfini et al., 2009). Unsurprisingly, mutations in several components of the transport machinery (e.g., dynein, cargo adaptors, LIS1, kinesin) have been linked to both neurodevelopmental and neurodegenerative diseases (Markus et al., 2020; Sleight et al., 2019). Neurons are especially susceptible to dysfunctions in transport regulation due to their highly elongated and extensively branched morphology. Thus, in order to understand the mechanisms underlying the establishment and maintenance of neuronal health and develop strategies to prevent or reduce the severity of disease, it is imperative that we decipher the mechanisms that can affect and regulate axonal transport.

Global Zn^{2+} increases had been shown acutely during ischemia (Koh et al., 1996; Granzotto et al., 2020) and chronically in Alzheimer’s disease patients (Deibel et al., 1996; Religa et al., 2006). Our findings suggest that such Zn^{2+} dyshomeostasis

may contribute to wide-scale transport defects. Further, this Zn^{2+} dyshomeostasis and the resulting effects on axonal transport may also alter the crucial anterograde delivery of NMNAT2 and STMN2 (axonal survival factors) into axons on vesicular organelles (Shin et al., 2012; Gilley and Coleman, 2010), thus resulting in axonal degeneration. Additionally, our results demonstrate that Zn^{2+} shares many common features with tau, a pathological marker of Alzheimer’s disease, in regulating microtubule-based processes. First, the predicted binding sites of Zn^{2+} on microtubules are adjacent to the binding sites for tau protein. Second, we show that Zn^{2+} can arrest both kinesin and dynein-mediated motility, which is similar to tau which can inhibit the function of kinesin, and to a lesser extent dynein (Chaudhary et al., 2018). Third, we find that Zn^{2+} demonstrates a dose-dependent increase in microtubule polymerization, while previous studies found that tau can also promote microtubule polymerization (Feizabadi et al., 2019). As such, abnormal Zn^{2+} elevation under pathological conditions could disrupt the proper localization of MAPs and importantly promote tau detachment from microtubules, thus increasing the chance for tau aggregates to form in the cytosol. In fact, Zn^{2+} has been shown to directly influence tau aggregation (Moreira et al., 2019; Singh et al., 2020; Huang et al., 2014).

Overall, our work supports existing hypotheses that Zn^{2+} imbalance may be a precursor to Alzheimer’s disease and other tauopathies (Craddock et al., 2012; Craven et al., 2018; Hu et al., 2017), while also revealing a possible mechanism of Zn^{2+} homeostasis for regulation of axonal transport and neuronal MAP function. From a broader perspective, this study corroborates a long-suspected signaling role of intracellular Zn^{2+} with the discovery that Zn^{2+} can directly regulate microtubule-based organellar trafficking, which is essential and required for diverse cellular processes in all eukaryotic cell types throughout the evolutionary spectrum.

Materials and methods

Animal care

Pregnant Sprague Dawley rats were purchased from Charles River (strain: 400). Animal treatment and maintenance were performed by the University of Denver Animal Facility (AAA-LAC accredited). All experimental procedures using animals were approved by the Institutional Animal Care and Use Committee (IACUC) of the University of Denver.

Plasmid generation

Expression plasmids were constructed using traditional molecular biological techniques and were all verified by sequencing. To construct LAMP1-mCherry, mCherry was PCR amplified from mCherry-Rab7a-7, LAMP1 was PCR amplified from LAMP1-RFP, and both were ligated into pcDNA3.1+. mCherry-Rab7a-7 was a gift from Michael Davidson (plasmid #55127; Addgene; <http://n2t.net/addgene:55127>; RRID:Addgene_55127). Lamp1-RFP (Sherer et al., 2003) was a gift from Walther Mothes (plasmid #1817; Addgene; <http://n2t.net/addgene:1817>; RRID:Addgene_1817). mCh-alpha-tubulin (Friedman et al., 2010) was a gift from Gia Voeltz (plasmid #49149; Addgene; <http://n2t.net>).

net/addgene:49149; RRID:Addgene_49149). EGFP-DCX (Tanaka et al., 2004) was a gift from Joseph Gleeson (plasmid #32852; Addgene; <http://n2t.net/addgene:32852>; RRID:Addgene_32852). pRK5-EGFP-tau (Hoover et al., 2010) was a gift from Karen Ashe (plasmid #46904; Addgene; <http://n2t.net/addgene:46904>; RRID:Addgene_46904). pEGFP-p150Glued (Watson and Stephens, 2006) was a gift from David Stephens (plasmid #36154; Addgene; <http://n2t.net/addgene:36154>; RRID:Addgene_36154). GFP-MAP1B (Scales et al., 2009) was a gift from Phillip Gordon-Weeks (plasmid #44396; Addgene; <http://n2t.net/addgene:44396>; RRID:Addgene_44396). pEGFP-Map7-fulllength (Metzger et al., 2012) was a gift from Edgar Gomes (plasmid #46076; Addgene; <http://n2t.net/addgene:46076>; RRID:Addgene_46076). mEmerald-MAP4-C-10 (Planchon et al., 2011) was a gift from Michael Davidson (plasmid #54152; Addgene; <http://n2t.net/addgene:54152>; RRID:Addgene_54152). MAP9 in pCR-XL-TOPO (#BC146864) was purchased from Transomic Technologies, and subcloned into pcDNA with an N-terminal EGFP tag. MAP2C in pENTR223-1 (#BC172263) was purchased from Transomic Technologies, and subcloned into pcDNA with an N-terminal EGFP tag. NPY-mCherry was a gift from Wolhard Almers (plasmid #67156; Addgene; <http://n2t.net/addgene:67156>; RRID:Addgene_67156). GW1-PercevalHR was a gift from Gary Yellen (plasmid #49082; Addgene; <http://n2t.net/addgene:49082>; RRID:Addgene_49082).

Primary rat hippocampal neuron culture and transfection

Primary hippocampal neurons were prepared from rat embryos at embryonic day 18 (E18) in dissection medium containing HBSS, 1 M HEPES buffer (pH 7.3) and 50 µg/ml gentamycin. The hippocampi were minced and treated with 1,000 U/ml papain added to the dissection medium and dissociated by trituration in 1 mg/ml DNase I. Cells were plated on 1 mg/ml poly-L-lysine-coated 10 mm round glass coverslips at a density of 20,000–25,000 cells/coverslip per dish in neuron plating medium (MEM supplemented with glucose and 5% FBS). After checking that cells were adhered, neuron plating medium was replaced with Neurobasal medium (Thermo Fisher Scientific) supplemented with 0.3× GlutaMAX (Thermo Fisher Scientific) and 1× B-27 (Thermo Fisher Scientific). Cultures were maintained at 37°C, 5% CO₂. Neurons were transfected between 5 and 10 d in vitro (DIV), using the Lipofectamine 3000 transfection kit (Thermo Fisher Scientific) in 500 µl Opti-MEM. The reagent-DNA mixture was incubated for a minimum of 25 min at room temperature before direct addition to the neuron imaging dishes. Before adding reagent-DNA, 1 ml media was removed from each imaging dish and syringe filtered with an equal volume of fresh neuron culture media (50:50 media). After incubation at 37°C for 4 h, neurons were washed three times with 1 ml prewarmed neuron culture media. Then, 2 ml of the 50:50 media was added to the neuron imaging dishes and they were incubated at 37°C until imaging.

Drug treatment and live cell imaging of neurons and analysis of axonal motility

Live cell imaging of neurons was performed two or more days after transfection. Neurons were washed and imaged in HEPES-

Buffered Hanks Balanced Salt Solution (HHBSS) lacking Ca²⁺ and Zn²⁺. For experiments in which Zn²⁺ influx was induced by depolarization, neurons were treated with Ca²⁺-free HHBSS supplemented with 50 mM KCl and 100 µM ZnCl₂ during the acquisition period (20 min in duration). For experiments in which chelation followed depolarization-induced Zn²⁺ influx, neurons were washed three times with Ca²⁺-free HHBSS, then treated with 100 µM TPEN and immediately imaged. For experiments in which Zn²⁺ influx was induced with pyrithione treatment, neurons were washed three times with Ca²⁺-free HHBSS and then treated with 100 µM ZnCl₂ and 2.5–5 µM pyrithione.

All live neuron imaging was performed on an inverted Nikon/Solamere CSUX1 spinning disc confocal microscope equipped with a 40×1.4 NA oil immersion objective, a Hamamatsu ×2 EMCCD camera, and a variable 1.0× or 1.5× OptiVar tube lens. Axonal motility imaging was performed in a LiveCell imaging chamber kept at 37°C, 5% CO₂, and 80% humidity. The microscope was controlled with MicroManager software and image analysis was performed using Fiji (Schindelin et al., 2012; see below for details on image analysis). To image lysosomal and mitochondrial, and Neuropeptide Y motility (via LAMP1-mCherry, mito-mCherry, or NPY-mCherry respectively), fluorescence images were acquired every 0.5–2.5 s, with 50–100 millisecond exposures with a 561 nm laser at 1–5 mW power.

To analyze organellar axon motility, image contrast of each movie was enhanced by first employing a bandpass filter to remove frequencies larger than 7 px and <2 px. Fiji's built in "Background subtraction" was then run using a five px rolling ball radius. Image stacks were then stabilized (if needed) using the Manual Drift Correction plugin for Fiji. Kymographs were generated using the Kymolyzer plugin (Basu et al., 2020), and background kymograph noise was removed using a custom code (ImageJ Macro Language). These kymographs were then analyzed using the KymoButler (Jakobs et al., 2019) plug-in for Mathematica (Wolfram Research, Inc.). Instantaneous velocities measured by the KymoButler plug-in were extracted using custom code (Wolfram Language) in order to get a more accurate description of motility, as the density of bidirectionally moving lysosomes reduced the accuracy of computer-generated track averages. Axons were manually traced back to their soma to confirm orientation, which was used to classify retrograde or anterograde motility. KymoButler-measured tracks with durations <4 s were also removed entirely from analysis to eliminate the measurement of kymograph noise artifacts. The proportion of anterograde, retrograde, and stationary organelles were calculated as previously reported (Lewis et al., 2016; Farfel-Becker et al., 2019; Celestino et al., 2022; Nassal et al., 2022).

Non-neuronal cell culture and transfection

HeLa cells and COS-7 cells (African Green Monkey fibroblast-like cell line) were maintained in high glucose Dulbecco's Modified Eagle Medium (DMEM) supplemented with 10% FBS. COS-7 cells were grown in 100 U/ml Penicillin G and 100 µg/ml Streptomycin on poly-D-lysine-coated coverslips. All cells were maintained at 37°C and 5% CO₂. HeLa and COS-7 cell transfections were performed with polyethyleneimine (PEI; dissolved

to 1 mg/ml in water at pH 7.2, with long-term storage at -20°C and short-term storage at 4°C). For each transfection, 3–6 μl of PEI and 1–1.25 μg of DNA were mixed in 250 μl Opti-MEM, incubated for >25 min at room temperature, then added to one imaging dish with cells (~ 40 – 50% confluent). Imaging dishes were incubated at 37°C until imaged as described above.

Zn^{2+} concentration measurement using genetically encoded fluorescent probes

For simultaneous analysis of Zn^{2+} concentrations and organellar motility, GZnP2 was co-transfected into HeLa cells or primary rat hippocampal neurons with either mito-mCherry or LAMP1-mCherry. After acquiring images to determine baseline Zn^{2+} concentration and motility, 100 μM TPEN was added to chelate Zn^{2+} . Cells were then washed three times to remove TPEN, treated with 100 μM ZnCl_2 , then treated with 2.5 μM pyrithione (as indicated on respective plots). GZnP2 fluorescence was acquired by excitation with 488 nm and collecting 525 nm emission. GZnP2 fluorescence intensity values were converted to Zn^{2+} concentrations using the equation

$$[\text{Zn}^{2+}] = K_d \left(\frac{(I - I_{\min})}{(I_{\max} - I)} \right)^{\frac{1}{n}},$$

where K_d is the Zn^{2+} equilibrium dissociation constant, n is the Hill coefficient, I is background-subtracted fluorescence intensity, and I_{\min} and I_{\max} are minimum and maximum fluorescence intensities, respectively. K_d and Hill coefficients were experimentally determined using purified GZnP2, which revealed $K_d = 352$ pM, and $n = 0.49$ (Fudge et al., 2018). Data points that yielded $[\text{Zn}^{2+}] > 100$ μM (no more than 3 data points out of 300+ total data points per cell) were removed from further analysis since theoretically cytosolic $[\text{Zn}^{2+}]$ shouldn't exceed the concentration of the exogenous buffer. Normalized motility values (for HeLa cells, see below) or direct speeds (for neuron axons, see Kymo-Butler methods above) were plotted against the calculated Zn^{2+} concentrations, and fit to a sigmoidal curve using JMP Pro 15.2.0 or KaleidaGraph (Synergy Software), which was used to calculate the Zn^{2+} IC_{50} concentration. Data were fit to sigmoidal curves using a standard dose-response curve,

$$y = d + \frac{(a - d)}{1 + \left(\frac{[\text{Zn}^{2+}]}{c} \right)^b},$$

where a is the upper asymptote, b is the growth rate, c is the IC_{50} , and d is the lower asymptote.

Organellar motility analysis in HeLa cells

The Total Motility plugin (De Vos and Sheetz, 2007) for Fiji was used to determine the relative motility of organellar structures. Images were binarized by automatic thresholding, then processed by the Total Motility plugin. Motility data were normalized to baseline using the equation

$$\% \text{Baseline Motility} = 100 \times \left(\frac{(x - x_{\min})}{(x_{\text{baseline}} - x_{\min})} \right),$$

where x equals the raw motility data output from the Total Motility plugin, x_{\min} equals the minimum raw motility data point, and x_{baseline} equals the average motility value for all baseline timepoints. The raw motility data output from the Total Motility plugin is the proportion of thresholded binary pixels that changed from one frame to the next, as a percentage of the total number of positive (white, non-background) pixels in that frame. Images of LAMP1-mCherry or mito-mCherry were acquired every 5 s with a 50–100 millisecond exposure of 561 nm laser excitation at 1–5 mW power. The raw motility output was normalized to average baseline motility for each cell. Extreme motility changes that were clearly due to observable stage shift (i.e., during drug addition) were removed from further analysis.

Lysosomal or mitochondrial motility was measured using the “Total Motility” plugin (De Vos and Sheetz, 2007) for ImageJ, which calculates the percentage of organellar movements by measuring the area of shifted mitochondria (or lysosomes) out of the total mitochondrial (or lysosomal) area for each acquisition time point in each cell.

Peroxisome dispersion assays and analysis in COS-7 cells

For rapalog-induced peroxisome dispersion assays, COS-7 cells were co-transfected with PEX3-mRFP-2xFKBP and either KIF5A(1-560)-mNG-FRB or KIF5C(1-559)-mNG-FRB, and imaged within 24 h as longer transfection resulted in altered localization of the PEX3 construct and cell morphology. Peroxisome dispersion assays were imaged on the Nikon/Solamere CSUX1 spinning disc confocal microscope as described above. For timelapse experiments, cells were imaged for a 5-min baseline, then 1 μM pyrithione and varying Zn^{2+} concentrations (as indicated) for 5 min. Finally, 100 nM Zotarolimus was added to induce heterodimerization, and cells were imaged for 25 min. Images were acquired every 10 s with a 50–200 ms exposure for both 488 and 561 nm laser excitation at 10 and 5 mW power, respectively. Custom code (ImageJ Macro Language) was used to detect PEX3-mRFP maxima and quantify average distance of peroxisomes from the center of the cell.

As a non-dispersed peroxisome control, COS-7 cells were treated with 2 μl DMSO for 5 min (vehicle control for pyrithione), then another 2 μl DMSO for 25 min (vehicle control for Zotarolimus). As a positive control, COS-7 cells were treated with 1 μl PTO for 5 min, 100 nM Zotarolimus for 25 min. Finally, to test the effect of Zn^{2+} , COS-7 cells were treated with 10 μM Zn^{2+} and 1 μM PTO for 5 min, 100 nM Zotarolimus for 25 min. After treatment, cells were fixed with 4% paraformaldehyde in 0.1 M PBS with 4% sucrose at 4°C for 10 min. Fixation was quenched with 0.1 M glycine for 5 min, then cells were washed with PBS and imaged. Custom code (ImageJ Macro Language) was used to measure fluorescence intensity of PEX3-mRFP as a function of distance from the geometric cell center.

Oblique illumination imaging of motor proteins and microtubules in COS-7 cells

COS-7 cells were co-transfected with KIF5A(1-560)-mNG-FRB and mCherry- α -tubulin, and imaged within 48 h. Images were taken using a ONI Nanoimager with oblique illumination

(55.1° illumination angle), 1–2% 488 nm laser power, 6–8% 561 nm laser power, and 25–100 ms exposure times.

Yeast dynein complex protein purification

Purification of the artificially dimerized (by glutathione-S-transferase, GST) minimal dynein motor fragment (GST-dynein^{MOTOR}-HaloTag) was performed as previously described (Marzo et al., 2020). Briefly, yeast cultures were grown in YPA supplemented with 2% glucose (for the intact dynein complex) or 2% galactose (for GST-dynein^{MOTOR}), harvested, washed with cold water, and then resuspended in a small volume of water. The resuspended cell pellets were drop frozen into liquid nitrogen and then lysed in a coffee grinder. After lysis, 0.25 volume of 4× lysis buffer (1× buffer: 30 mM HEPES, pH 7.2, 50 mM potassium acetate, 2 mM magnesium acetate, 10% glycerol, 0.2 mM EGTA, 1 mM DTT, 0.1 mM Mg-ATP, 0.5 mM Pefabloc SC) was added, and the lysate was clarified at 22,000 × g for 20 min. The supernatant was then incubated with IgG sepharose 6 fast flow resin (GE) for 1 h at 4°C, which was subsequently washed three times in lysis buffer, and twice in TEV buffer (50 mM Tris, pH 8.0, 150 mM potassium acetate, 2 mM magnesium acetate, 1 mM EGTA, 0.005% Triton X-100, 10% glycerol, 1 mM DTT, 0.1 mM Mg-ATP, 0.5 mM Pefabloc SC). The protein was then incubated in TEV buffer supplemented with TEV protease for 1 h at 16°C. Following TEV digest, the solution was collected, and the resulting protein solution was aliquoted, flash frozen in liquid nitrogen, and stored at –80°C.

Microtubule binding domain (MTBD) SRS fusion protein purification

Purification of the SRS fusion proteins (GFP-SRS-dyneinMTBD and GFP-SRS-kinesinMTBD) were performed essentially as described (Ecklund et al., 2017). Briefly, IPTG-induced *E. coli* BL21 were harvested, washed with cold water, resuspended in cold lysis buffer (30 mM HEPES, pH 8.0, 50 mM potassium acetate, 2 mM magnesium acetate, 10% glycerol, 10 mM imidazole, 5 mM beta-mercaptoethanol) supplemented with cOmplete EDTA-free protease inhibitor cocktail, and then lysed by sonication (5 × 30 s pulses) with 1 min on ice between each pulse. The clarified lysate was incubated with Ni-NTA agarose (Qiagen) for 1 h at 4°C, washed three times in lysis buffer, and the bound protein was eluted with elution buffer (30 mM HEPES, pH 8.0, 50 mM potassium acetate, 2 mM magnesium acetate, 10% glycerol, 200 mM imidazole, 5 mM beta-mercaptoethanol). Peak fractions were pooled and applied to a Superdex 200 10/300 gel filtration column (GE; using an AKTA fast protein liquid chromatography system, or FPLC) equilibrated in lysis buffer. Peak gel filtration fractions were pooled, concentrated (to ≥ 47 μM), aliquoted, and drop frozen in liquid nitrogen.

Preparation of Zn²⁺/chelator-buffered solutions

Buffers with precisely controlled Zn²⁺ concentrations were prepared according to previous established protocol (Qin et al., 2011) for the in vitro motor ATPase assays. Solutions with Zn²⁺ from picomolar to micromolar concentrations were made by a pH-titration method. As indicated below, different Zn²⁺ chelators (EGTA and HEEDTA) and competing metal ions (Ca²⁺ or

Sr²⁺) were used to buffer Zn²⁺ at pH 7.2 (for in vitro motility assays) or pH 6.9 (for in vitro microtubule polymerization assays).

To obtain free Zn²⁺ concentrations in the low picomolar range, we used HEEDTA with no competing metal ions. The stability constant of the Zn²⁺ complex of HEEDTA is: pK₁ = 9.81, pK₂ = 5.37, logK (ZnL) = 14.6. Two separate 100× stock solutions were made: 0.1 M HEEDTA (Buffer B4), and 0.1 M ZnCl₂ + 0.1 M HEEDTA (Buffer A4). [HEEDTA]_t was set at 1 mM and [Zn²⁺]_t was varied from 0.1 to 0.9 mM in 0.1 mM increments by mixing 1× A4 and B4 buffers at different ratios to obtain the free Zn²⁺ concentrations shown in Table 1.

To obtain free Zn²⁺ concentrations in the high picomolar to low nanomolar range, we used EGTA with no competing metal ions. The stability constant of the Zn²⁺ complex of EGTA is pK₁ = 9.40, pK₂ = 8.78, logK(ZnL) = 12.6. Two separate 100× stock solutions were made: 0.1 M EGTA (Buffer B3), and 0.1 M ZnCl₂ + 0.1 M EGTA (Buffer A3). [EGTA]_t was set at 1 mM and [Zn²⁺]_t was varied from 0.1 to 0.9 mM in 0.1 mM increments by mixing 1× A3 and B3 buffers at different ratios to obtain the free Zn²⁺ concentrations shown in Table 2.

To obtain free Zn²⁺ concentrations in the nanomolar to low micromolar range, we used EGTA with Sr²⁺ as a competing metal ion. The stability constant of the Zn²⁺ complex of EGTA is: pK₁ = 9.40, pK₂ = 8.78, logK(SrL) = 8.50, logK(ZnL) = 12.6. Two separate 100× stock solutions were made: 0.1 M EGTA + 0.2 M SrCl₂ (Buffer B2), and 0.1 M ZnCl₂ + 0.1 M EGTA + 0.2 M SrCl₂ (Buffer A2). [EGTA]_t and [Sr]_t was set at 1 mM, and [Zn²⁺]_t was varied from 0.1 to 0.9 mM in 0.1 mM increments by mixing 1× A2 and B2 buffers at different ratios to obtain the free Zn²⁺ concentrations shown in Table 3.

To obtain free Zn²⁺ concentrations in the micromolar range, we used EGTA with Ca²⁺ as a competing metal ion. The stability constant of Zn²⁺ complex of EGTA is: pK₁ = 9.40, pK₂ = 8.78, logK [CaL] = 10.86, logK(ZnL) = 12.6. Two separate 100× stock solutions were made: 0.1 M EGTA + 0.2 M CaCl₂ (Buffer B1), and 0.1 M ZnCl₂ + 0.1 M EGTA + 0.2 M CaCl₂ (Buffer A1). [EGTA]_t and [Ca]_t was set at 1 mM, and [Zn²⁺]_t was varied from 0.1 to 0.9 mM in 0.1 mM increments by mixing 1× A1 and B1 buffers at different ratios to obtain the free Zn²⁺ concentrations shown in Table 4.

In vitro motor ATPase assays

For in vitro motor protein ATPase assays, the EnzChek Phosphate Assay Kit (#E-6646; Thermo Fisher Scientific) was used. Pre-formed, taxol-stabilized microtubules and recombinant human kinesin (KIF5A) were purchased from Cytoskeleton. A minimally processive, artificially dimerized yeast dynein fragment (GST-dynein₃₃₁) was purified as described above. Motor protein assay buffer (MPAB: 30 mM HEPES, pH 7.2, 50 mM potassium acetate, 2 mM magnesium acetate, 10% glycerol) was prepared using Chelex-treated H₂O to remove all metal ion contaminants. 10 μM taxol, 500 μM DTT, 200 μM MESG, 1 U/ml purine nucleoside phosphorylase, 2 mM ATP, 1 μM taxol-stabilized microtubules, and 1× buffered zinc solutions (described above) were added to MPAB, then plated into a 96 well plate. Plates were spun down at 2,250 rpm for 2 min, then incubated at room temperature for 10 min. Plates were read on a

Table 1. Low picomolar buffered zinc solutions

1× Buffer A4	1	2	3	4	5	6	7	8	9
1× Buffer B4	9	8	7	6	5	4	3	2	1
[Zn] _t (mM)	0.1	0.2	0.3	0.4	0.5	0.6	0.7	0.8	0.9
[Zn ²⁺] (pM)	0.29	0.66	1.1	1.8	2.6	4.0	6.2	10.5	23.8
	-	-	-	-	-	-	-	-	48
									pH 6.9

Synergy HTX Multi-Mode Microplate Reader (BioTek), collecting absorbance at 360 nm every 10 s. Background phosphate release was measured for 5 min, then either 5 nM GST-dynein₃₃₁ or 10 nM KIF5A was added to each well, and absorbance at 360 nm was read for an additional 10–20 min. A phosphate standard was collected as described in the EnzChek Phosphate Assay Kit.

Real-time measurement of in situ ATP/ADP ratio in COS-7 cells

COS-7 cells were transfected with the ratiometric sensor GW-PercevalHR and imaged 48 h after transfection. Experiments were performed in HHBSS buffer. A 5-min baseline was recorded, followed by a 5-min 100 μM ZnCl₂ and 2.5 μM PTO treatment, 5-min washout, and 15-min 2.5–5 μM oligomycin treatment. Images were acquired at 10 s intervals. PercevalHR was excited at 405 and 488 nm, and emission was measured at 525 nm.

In vitro motor MTBD-microtubule binding assays

Briefly, flow chambers constructed using slides and plasma cleaned and silanized coverslips, attached with double-sided adhesive tape were coated with either anti-tubulin antibody (8 μg/ml, YL1/2; Accurate Chemical & Scientific Corporation), then blocked with 1% Pluronic F-127 (Thermo Fisher Scientific). Taxol stabilized microtubules assembled from porcine tubulin (Cytoskeleton) were introduced into the chamber. Following a 5–10 min incubation, the chamber was washed with dynein lysis buffer supplemented with 20 μM taxol. Mixtures of dynein or kinesin fragments diluted in motility buffer (30 mM HEPES, pH 7.2, 50 mM potassium acetate, 2 mM magnesium acetate, 10% glycerol, 1 mM DTT) supplemented with 20 μM taxol with or without the 100 μM ZnCl₂ were flowed into the chambers, after which the chambers were immediately imaged. TIRFM images were acquired using a 1.49 NA 100× TIRF objective on a Nikon Ti-E inverted microscope equipped with a Ti-S-E motorized stage, piezo Z-control (Physik Instrumente), and an iXon ×3 DU897 cooled EM-CCD camera (Andor). A 488 nm laser (Coherent) was used along with a multi-pass quad

filter cube set (C-TIRF for 405/488/561/638 nm; Chroma) and emission filters mounted in a filter wheel (525/50 nm; Chroma). We imaged label-free microtubules using interference reflection microscopy (IRM) as previously described (Mahamdeh et al., 2018). To compare the relative microtubule-binding capacity of a given protein fragment (e.g., GFP-SRS-dyneinMTBD or GFP-SRS-kinesinMTBD), imaging conditions were kept constant for the minus and plus ZnCl₂ conditions (i.e., laser power and camera exposures). Quantitation of the relative microtubule-binding was performed using ImageJ software (National Institutes of Health). Fluorescence intensities were measured along microtubules (“signal”), and adjacent to microtubules (“background”). Mean corrected pixel intensity was determined by subtracting background from signal, then normalized to the average fluorescence intensities for the 0 Zn²⁺ condition.

In vitro microtubule polymerization assays

For in vitro microtubule polymerization assays, the traditional turbidity assay was used to monitor microtubule polymerization via absorbance at 340 nm with minor modifications. Purified porcine tubulin was purchased from Cytoskeleton and reconstituted to 10 mg/ml in microtubule assay buffer (“MTAB”: 80 mM PIPES, pH 6.9, 2 mM MgCl₂, in Chelex-treated H₂O) supplemented with 1 mM GTP. Microtubule reaction mix (MTAB, 5% glycerol, 2 mM GTP, and 5 mg/ml tubulin) was prepared on ice. 1× buffered Zn²⁺ solutions (described above) were plated into pre-chilled 96 well half-area plates, followed by microtubule reaction mix (50 μl total reaction volume). Plates were kept on ice until they were read on a Synergy HTX Multi-Mode Microplate Reader (BioTek), prewarmed to 37°C, collecting absorbance at 340 nm every 20 s for 60 min.

In vitro microtubule-Zn²⁺ binding assays

Pre-polymerized microtubules were purchased from Cytoskeleton. Varying concentrations of microtubules were added to buffer (15 mM PIPES, 5 mM MgCl₂, pH 7.0) supplemented with 10 μM taxol and 500 μM DTT. 1 μM ZnCl₂ (prepared with

Table 2. High picomolar to low nanomolar buffered zinc solutions

1× Buffer A3	1	2	3	4	5	6	7	8	9
1× Buffer B3	9	8	7	6	5	4	3	2	1
[Zn] _t (mM)	0.1	0.2	0.3	0.4	0.5	0.6	0.7	0.8	0.9
[Zn ²⁺] (nM)	0.29	0.66	1.1	1.7	2.6	3.9	6.1	10.5	23.6
	1.1	-	-	-	-	-	-	-	93.0
									pH 6.9

Table 3. Nanomolar to low micromolar buffered zinc solutions

1× Buffer A2	1	2	3	4	5	6	7	8	9
1× Buffer B2	9	8	7	6	5	4	3	2	1
[Zn] _t (mM)	0.1	0.2	0.3	0.4	0.5	0.6	0.7	0.8	0.9
[Zn ²⁺] (nM)	9.7	23.8	44.2	74.1	119	190	315	570	1,340
	-	-	-	-	-	-	-	570	1,340
									pH 6.9

Chelex-treated H₂O) was then added, and the reaction was incubated for 10 min. 1 μM FluoZin-3 tetrapotassium salt (Thermo Fisher Scientific) was then added to each reaction, plated into a 96-well plate and incubated at room temperature for 10 min. Fluorescence was measured using a Synergy HTX Multi-Mode Microplate Reader (BioTek), collecting fluorescence every 30 s at 525 nm emission using a 488 nm excitation, for 5 min. As an internal control, 250 μM TPEN was added to each well to chelate all Zn²⁺ and plates were measures for 20 min, or until a fluorescent minimum plateau was reached. Data was normalized by subtracting the minimum post-TPEN fluorescence.

In situ analysis of KIF5A and MAP interaction with microtubules

COS-7 cells were co-transfected with mCherry-α-tubulin and either KIF5A(1-560)-EGFP, EGFP-DCX, EGFP-tau, EGFP-MAP2C, GFP-MAP1B, EGFP-p150Glued, mEmerald-MAP4, EGFP-MAP7, or EGFP-MAP9 and imaged 24–48 h post-transfection on the Nikon/Solamere CSUX1 spinning disc confocal microscope as described above. Still images of several cells at recorded stage positions were taken before time-lapse imaging. Cells were imaged for a 5-min baseline, then treated with metals and/or ionophores (as indicated) for 5 min. Still images of the same cells at the recorded stage positions were taken after the initial timelapse recording. For cells treated with 20 μM ZnCl₂, Zn²⁺ was subsequently chelated with 100 μM TPEN and cells were imaged for 5 min. Finally, still images of the same cells at the recorded stage positions were taken after the TPEN treatment. Timelapse images were acquired every 10–20 s with a 50–200 ms exposure for both 488 and 561 nm laser excitation at 10 and 5 mW power, respectively.

The “Tubeness” analysis plugin for ImageJ was used to quantify microtubule morphology of MAPs (σ value = 0.1425–0.216, appropriate for the micron/pixel calibration for each image’s magnification. Average tubeness for each cell was recorded at baseline, and each subsequent treatment, with values normalized to the baseline tubeness for each cell.

For depolarization experiments, primary hippocampal neurons (DIV 10–16) were depolarized for 5 min with 50 mM KCl in

the presence or absence of 100 μM ZnCl₂ in HHBSS lacking Ca²⁺. Neurons were immediately fixed with ice-cold methanol for 10 min at –20°C to simultaneously permeabilize neurons and fix cells in a manner which would preserve microtubules and MAP interactions on microtubules. Fixed cells were blocked with 3% BSA for 30 min, then immediately immunostained (no PBS wash) with anti-tau polyclonal primary antibody (reactive to human, mouse, rat) raised in rabbit (IgG isotype) at a 1:700 dilution for 1 h at room temperature or overnight at 4°C. Cells were then washed with PBS, and re-blocked with 3% BSA for 15 min. Cells were then incubated with goat anti-Rabbit IgG (H+L) Cross-Adsorbed secondary antibody conjugated to Alexa Fluor 488 (A-11008) at a 1:500 dilution and beta Tubulin loading control monoclonal antibody conjugated to Alexa Fluor 555 (MA5-16308) at a 1:250 dilution for 45 min. Cells were finally washed with PBS then stained with 600 nM DAPI and imaged on the Nikon/Solamere CSUX1 spinning disc confocal microscope as described above. Multichannel images were taken across a 1 mm² area of the neuron culture for each dish and stitched together using the built-in Fiji “Stitching” plugin. Custom code (ImageJ Macro Language) was used to analyze the individual images to segment microtubule-positive areas, primarily axons, and measure average fluorescence intensity of Alexa Fluor 488. COS7-cells used for endogenous tubulin expression control experiments were first washed with Ca²⁺-free HHBSS then treated with either 20 μM ZnCl₂ + 2.5 μM PTO or 2.5 μM PTO alone for 5 min. The cells were then methanol fixed in the same manner, blocked with 3% BSA for 30 min at 4°C, and incubated with beta Tubulin loading control monoclonal antibody conjugated to Alexa Fluor 555 (MA5-16308) at a 1:250 dilution for 1 h at 4°C. Cells were then washed with PBS, DAPI stained, and imaged as described above.

Analysis of MAP interaction and predicted Zn²⁺ binding sites on microtubules

Molecular graphics and analyses were performed with UCSF Chimera (Pettersen et al., 2004), developed by the Resource for Biocomputing, Visualization, and Informatics at the University of California, San Francisco, with support from NIH P41-GM103311.

Table 4. Micromolar buffered zinc solutions

1× Buffer A1	1	2	3	4	5	6	7	8	9
1× Buffer B1	9	8	7	6	5	4	3	2	1
[Zn] _t (mM)	0.1	0.2	0.3	0.4	0.5	0.6	0.7	0.8	0.9
[Zn ²⁺] (μM)	2.7	6.7	12.2	20.0	30.5	45.4	66.3	95.2	135

Previously published cryo-EM microtubule reconstruction models (PDB ID: 6EVY) were used for MAP interaction and Zn^{2+} binding prediction analysis. The only available cryo-EM reconstruction models of microtubule-bound MAPs analyzed were DCX (PDB ID: 6REV), tau (PDB ID: 6CVN), kinesin microtubule binding domain (PDB ID: 3J8X), and cytoplasmic dynein microtubule binding domain (PDB ID: 6RZB). Individually, the microtubule-bound MAPs were analyzed using the Protein-Ligand Interaction Profiler (PLIP; Salentin et al., 2015), where the MAP was specified as the ligand and all inter-chain interactions (hydrophobic interactions, hydrogen bonds, and salt bridges) between the ligand and α -tubulin or β -tubulin were analyzed. Using Chimera, α -tubulin and β -tubulin residues identified by PLIP were colored to correspond with the MAP(s) that interacted with the residue.

Zn^{2+} binding prediction analysis of α -tubulin or β -tubulin was performed using the MIB (Metal Ion-Binding Site Prediction and Docking) Server (Lin et al., 2016). Chain A (α -tubulin) and Chain B (β -tubulin) from the cryo-EM microtubule reconstruction model (PDB ID: 6EVY) were run individually. α -tubulin and β -tubulin residues identified by MIB with a score >0 were colored using the “Render by Attribute” interface.

Measurement of microtubule acetylation levels in situ

Hippocampal neurons at DIV 11–13 were first washed with Ca^{2+} free HHBSS, then treated with 50 mM KCl alone or 50 mM KCl + 100 μM ZnCl_2 for 5 min. Cells were then methanol fixed as previously described, then blocked with 3% BSA at 4°C for 30 min. Fixed cells were first incubated with acetyl- α Tubulin (Lys40) monoclonal antibody conjugated to Alexa Fluor 488 (6-11 B-1) at a 1:100 dilution for 1 h at room temperature. Cells were then washed with PBS, 5 min each wash, and then incubated with beta Tubulin loading control monoclonal antibody conjugated to Alexa Fluor 555 (MA5-16308) at a 1:250 dilution at room temperature for 45 min. Cells were then washed with PBS, DAPI stained, and imaged as described above. Still images were taken at 10 different positions per dish at 20 \times and 60 \times magnification. For images taken at 20 \times magnification, 6 axons were traced in each still image. The average fluorescence intensity for each axon ROI was measured for both 488 and 561 channels, and data for acetylated- α tubulin was normalized to beta-tubulin.

Analysis of cell health in COS-7 cells and hippocampal neurons

COS-7 cells were transfected with LAMP1-mCherry and imaged 48 h after transfection. Hippocampal neurons were transfected with mito-mCherry on DIV 5–6 and imaged DIV 10–14. On the day of imaging, cells were washed with Ca^{2+} -free HHBSS, then incubated with Hoechst stain for 10 min. Cells were washed again with Ca^{2+} -free HHBSS before imaging. For COS-7 cells, a 5-min baseline, 5 min 20 μM ZnCl_2 + 2.5 μM PTO treatment, washout, and 100 μM TPEN treatment was recorded. For hippocampal neurons, a 10-min baseline, 20-min 50 mM KCl + 100 μM ZnCl_2 treatment, washout, and 100 μM TPEN treatment was recorded. Representative images are acquired after the indicated treatment.

Data analysis and statistics

Imaging data were analyzed with Fiji (ImageJ, National Institutes of Health) and raw data output from Fiji were analyzed

using Microsoft Excel in combination with JMP software (JMP, Version 15.2.0. SAS Institute Inc.), and Mathematica (Wolfram Research, Inc., Version 12.1, Champaign, IL [2020]). Statistical analysis was performed using Excel or JMP software, using the appropriate statistical tests. All unpaired t tests were preceded by an F test to analyze variance equality. t tests were then performed with consideration for the determined variance equality or inequality. Least-squares regression with comparisons across all groups used restricted maximum likelihood estimation (REML) and post-hoc multiple comparisons used Tukey HSD. For parametric tests, data distribution was assumed to be normal but this was not formally tested. All measurements were taken from distinct samples. No region of interest (ROI) was measured repeatedly. When selecting a ROI in the soma for cytosolic sensors that were also present in the nucleus, care was taken to avoid selecting nuclear areas. For time traces of fluorescence intensity, background fluorescence was subtracted from ROIs. For single wavelength sensors, changes in fluorescence intensity ($\Delta F = F - F_0$) were normalized to the baseline preceding the 0-s time point (F_0), indicated as $\Delta F/F_0$.

Online supplemental material

Fig. S1 shows the inhibition effects of Zn^{2+} on mitochondria and dense core vesicles in primary hippocampal neurons. Fig. S2 shows that Zn^{2+} can inhibit lysosomal and mitochondrial motility in HeLa cells. Fig. S3 shows that Zn^{2+} can dose-dependently inhibit kinesin ATPase activity and dynein ATPase activity in vitro without changing intracellular ATP/ADP levels. Fig. S4 shows that Zn^{2+} dissociates DCX from microtubules without affecting endogenous microtubule morphologies and cell health. Fig. S5 shows that Zn^{2+} dissociates endogenous tau from microtubules in neurons without affecting microtubule acetylation. Table S1 shows statistical analysis of ion effects on DCX decoration of microtubules. Table S2 shows statistical analysis of ion effects on Tau decoration of microtubules. Table S3 shows statistical analysis of ion effects on MAP2C decoration of microtubules. Table S4 shows statistical analysis of Zn^{2+} effect on MAP decoration of microtubules.

Acknowledgments

This work was funded by the National Institutes of Health (R01NS110590 to Y. Qin; R01GM118492 and R35GM139483 to S.M. Markus; R35GM131744 to K. Verhey)

Author contributions: Conceptualization, T.F. Minckley, S.M. Markus, and Y. Qin; Methodology, T.F. Minckley, D.H. Fudge, K. Verhey, S.M. Markus, and Y. Qin; formal analysis, T.F. Minckley, L.A. Salvagio, and S.M. Markus; investigation, T.F. Minckley, L.A. Salvagio, D.H. Fudge, S.M. Markus; resources, K. Verhey, S.M. Markus, and Y. Qin; supervision, Y. Qin; writing and editing, T.F. Minckley, L.A. Salvagio, S.M. Markus, and Y. Qin.

Disclosures: The authors declare no competing interests exist.

Submitted: 22 August 2022

Revised: 31 March 2023

Accepted: 11 May 2023

References

- Adalbert, R., A. Kaieda, C. Antoniou, A. Loreto, X. Yang, J. Gilley, T. Hoshino, K. Uga, M.T. Makhija, and M.P. Coleman. 2020. Novel HDAC6 inhibitors increase tubulin acetylation and rescue axonal transport of mitochondria in a model of charcot-marie-tooth type 2F. *ACS Chem. Neurosci.* 11:258–267. <https://doi.org/10.1021/acscchemneuro.9b00338>
- Andreini, C., L. Banci, I. Bertini, and A. Rosato. 2006. Counting the zinc-proteins encoded in the human genome. *J. Proteome Res.* 5:196–201. <https://doi.org/10.1021/pr050361j>
- Bacchella, C., S. Gentili, D. Bellotti, E. Quartieri, S. Draghi, M.C. Baratto, M. Remelli, D. Valensin, E. Monzani, S. Nicolis, et al. 2020. Binding and reactivity of copper to R₁ and R₃ fragments of tau protein. *Inorg. Chem.* 59:274–286. <https://doi.org/10.1021/acs.inorgchem.9b02266>
- Basu, H., L. Ding, G. Pekkurnaz, M. Cronin, and T.L. Schwarz. 2020. Kymolyzer, a semi-autonomous kymography tool to analyze intracellular motility. *Curr. Protoc. Cell Biol.* 87:e107. <https://doi.org/10.1002/cpcb.107>
- Bellomo, E., A. Massarotti, C. Hogstrand, and W. Maret. 2014. Zinc ions modulate protein tyrosine phosphatase 1B activity. *Metallomics*. 6: 1229–1239. <https://doi.org/10.1039/C4MT00086B>
- Bodakuntla, S., X. Yuan, M. Genova, S. Gadadhar, S. Leboucher, M.C. Birling, D. Klein, R. Martini, C. Janke, and M.M. Magiera. 2021. Distinct roles of α - and β -tubulin polyglutamylation in controlling axonal transport and in neurodegeneration. *EMBO J.* 40:e108498. <https://doi.org/10.15252/emboj.2021108498>
- Böhm, K.J. 2017. Toxic effects of zinc ions on kinesin - potential molecular cause of impaired intracellular transport. *Toxicol. Lett.* 268:58–62. <https://doi.org/10.1016/j.toxlet.2017.01.013>
- Carter, A.P., J.E. Garbarino, E.M. Wilson-Kubalek, W.E. Shipley, C. Cho, R.A. Milligan, R.D. Vale, and I.R. Gibbons. 2008. Structure and functional role of dynein's microtubule-binding domain. *Science*. 322:1691–1695. <https://doi.org/10.1126/science.1164424>
- Celestino, R., J.B. Gama, A.F. Castro-Rodrigues, D.J. Barbosa, H. Rocha, E.A. d'Amico, A. Musacchio, A.X. Carvalho, J.H. Morais-Cabral, and R. Gassmann. 2022. JIP3 interacts with dynein and kinesin-1 to regulate bidirectional organelle transport. *J. Cell Biol.* 221:e202110057. <https://doi.org/10.1083/jcb.202110057>
- Chaudhary, A.R., F. Berger, C.L. Berger, and A.G. Hendricks. 2018. Tau directs intracellular trafficking by regulating the forces exerted by kinesin and dynein teams. *Traffic*. 19:111–121. <https://doi.org/10.1111/tra.12537>
- Craddock, T.J., J.A. Tuszynski, D. Chopra, N. Casey, L.E. Goldstein, S.R. Hameroff, and R.E. Tanzi. 2012. The zinc dyshomeostasis hypothesis of Alzheimer's disease. *PLoS One*. 7:e33552. <https://doi.org/10.1371/journal.pone.0033552>
- Craven, K.M., W.R. Kochen, C.M. Hernandez, and J.M. Flinn. 2018. Zinc exacerbates tau pathology in a tau mouse model. *J. Alzheimers Dis.* 64: 617–630. <https://doi.org/10.3233/JAD-180151>
- De Vos, K.J., and M.P. Sheetz. 2007. Visualization and quantification of mitochondrial dynamics in living animal cells. *Methods Cell Biol.* 80: 627–682. [https://doi.org/10.1016/S0091-679X\(06\)80030-0](https://doi.org/10.1016/S0091-679X(06)80030-0)
- Deibel, M.A., W.D. Ehmann, and W.R. Markesbery. 1996. Copper, iron, and zinc imbalances in severely degenerated brain regions in Alzheimer's disease: Possible relation to oxidative stress. *J. Neurol. Sci.* 143:137–142. [https://doi.org/10.1016/S0022-510X\(96\)00203-1](https://doi.org/10.1016/S0022-510X(96)00203-1)
- Dixit, R., J.L. Ross, Y.E. Goldman, and E.L. Holzbaur. 2008. Differential regulation of dynein and kinesin motor proteins by tau. *Science*. 319: 1086–1089. <https://doi.org/10.1126/science.1152993>
- Du, W., M. Gu, M. Hu, P. Pinchi, W. Chen, M. Ryan, T. Nold, A. Bannaga, and H. Xu. 2021. Lysosomal Zn²⁺ release triggers rapid, mitochondria-mediated, non-apoptotic cell death in metastatic melanoma. *Cell Rep.* 37:109848. <https://doi.org/10.1016/j.celrep.2021.109848>
- Dubey, J., N. Ratnakaran, and S.P. Koushika. 2015. Neurodegeneration and microtubule dynamics: Death by a thousand cuts. *Front. Cell. Neurosci.* 9: 343. <https://doi.org/10.3389/fncel.2015.00343>
- Ecklund, K.H., T. Morisaki, L.G. Lammers, M.G. Marzo, T.J. Stasevich, and S.M. Markus. 2017. Shet affects dynein through direct interactions with the microtubule and the dynein microtubule-binding domain. *Nat. Commun.* 8:2151. <https://doi.org/10.1038/s41467-017-02004-2>
- Eron, S.J., D.J. MacPherson, K.B. Dagbay, and J.A. Hardy. 2018. Multiple mechanisms of zinc-mediated inhibition for the apoptotic caspases-3, -6, -7, and -8. *ACS Chem. Biol.* 13:1279–1290. <https://doi.org/10.1021/acscchembio.8b00064>
- Even, A., G. Morelli, L. Broix, C. Scaramuzzino, S. Turchetto, I. Gladwyn-Ng, R. Le Bail, M. Shilian, S. Freeman, M.M. Magiera, et al. 2019. ATAT1-enriched vesicles promote microtubule acetylation via axonal transport. *Sci. Adv.* 5:eaax2705. <https://doi.org/10.1126/sciadv.aax2705>
- Fan, R., and K.O. Lai. 2022. Understanding how kinesin motor proteins regulate postsynaptic function in neuron. *FEBS J.* 289:2128–2144. <https://doi.org/10.1111/febs.16285>
- Farfel-Becker, T., J.C. Roney, X.T. Cheng, S. Li, S.R. Cuddy, and Z.H. Sheng. 2019. Neuronal soma-derived degradative lysosomes are continuously delivered to distal axons to maintain local degradation capacity. *Cell Rep.* 28:51–64.e4. <https://doi.org/10.1016/j.celrep.2019.06.013>
- Feizabadi, M.S., M.A.V. Hernandez, J.B. Breslin, and I.I. Akintola. 2019. The regulatory effect of Tau protein on polymerization of MCF7 microtubules in vitro. *Biochem. Biophys. Rep.* 17:151–156. <https://doi.org/10.1016/j.bbrep.2018.12.010>
- Foster, A.W., D. Osman, and N.J. Robinson. 2014. Metal preferences and metallation. *J. Biol. Chem.* 289:28095–28103. <https://doi.org/10.1074/jbc.R114.588145>
- Fransson, S., A. Ruusala, and P. Aspenström. 2006. The atypical Rho GTPases Miro-1 and Miro-2 have essential roles in mitochondrial trafficking. *Biochem. Biophys. Res. Commun.* 344:500–510. <https://doi.org/10.1016/j.bbrc.2006.03.163>
- Friedman, J.R., B.M. Webster, D.N. Mastronarde, K.J. Verhey, and G.K. Voeltz. 2010. ER sliding dynamics and ER-mitochondrial contacts occur on acetylated microtubules. *J. Cell Biol.* 190:363–375. <https://doi.org/10.1083/jcb.200911024>
- Fu, X., K.J. Brown, C.C. Yap, B. Winckler, J.K. Jaiswal, and J.S. Liu. 2013. Doublecortin (Dcx) family proteins regulate filamentous actin structure in developing neurons. *J. Neurosci.* 33:709–721. <https://doi.org/10.1523/JNEUROSCI.4603-12.2013>
- Fudge, D.H., R. Black, L. Son, K. Lejeune, and Y. Qin. 2018. Optical recording of Zn²⁺ dynamics in the mitochondrial matrix and intermembrane space with the GZnP2 sensor. *ACS Chem. Biol.* 13:1897–1905. <https://doi.org/10.1021/acscchembio.8b00319>
- Gibbons, I.R., J.E. Garbarino, C.E. Tan, S.L. Reck-Peterson, R.D. Vale, and A.P. Carter. 2005. The affinity of the dynein microtubule-binding domain is modulated by the conformation of its coiled-coil stalk. *J. Biol. Chem.* 280: 23960–23965. <https://doi.org/10.1074/jbc.M501636200>
- Gilley, J., and M.P. Coleman. 2010. Endogenous Nmnat2 is an essential survival factor for maintenance of healthy axons. *PLoS Biol.* 8:e1000300. <https://doi.org/10.1371/journal.pbio.1000300>
- Grabrucker, A.M., M.J. Knight, C. Proepper, J. Bockmann, M. Joubert, M. Rowan, G.U. Nienhaus, C.C. Garner, J.U. Bowie, M.R. Kreutz, et al. 2011. Concerted action of zinc and ProSAP/Shank in synaptogenesis and synapse maturation. *EMBO J.* 30:569–581. <https://doi.org/emboj.2010.336>
- Granzotto, A., L.M.T. Canzoniero, and S.L. Sensi. 2020. A neurotoxic Ménage-à-trois: Glutamate, calcium, and zinc in the excitotoxic cascade. *Front. Mol. Neurosci.* 13:600089. <https://doi.org/10.3389/fnmol.2020.600089>
- Guedes-Dias, P., J.J. Nirschl, N. Abreu, M.K. Tokito, C. Janke, M.M. Magiera, and E.L.F. Holzbaur. 2019. Kinesin-3 responds to local microtubule dynamics to target synaptic cargo delivery to the presynapse. *Curr. Biol.* 29:268–282.e8. <https://doi.org/10.1016/j.cub.2018.11.065>
- Gyparakis, M.T., A. Arab, E.M. Sorokina, A.N. Santiago-Ruiz, C.H. Bohrer, J. Xiao, and M. Lakadamyali. 2021. Tau forms oligomeric complexes on microtubules that are distinct from tau aggregates. *Proc. Natl. Acad. Sci. USA*. 118:e2021461118. <https://doi.org/10.1073/pnas.2021461118>
- Hancock, W.O., and J. Howard. 1999. Kinesin's processivity results from mechanical and chemical coordination between the ATP hydrolysis cycles of the two motor domains. *Proc. Natl. Acad. Sci. USA*. 96: 13147–13152. <https://doi.org/10.1073/pnas.96.23.13147>
- Hirokawa, N., Y. Noda, Y. Tanaka, and S. Niwa. 2009. Kinesin superfamily motor proteins and intracellular transport. *Nat. Rev. Mol. Cell Biol.* 10: 682–696. <https://doi.org/10.1038/nrm2774>
- Hogstrand, C., P.M. Verboost, and S.E. Wendelaar Bonga. 1999. Inhibition of human erythrocyte Ca²⁺-ATPase by Zn²⁺. *Toxicology*. 133:139–145. [https://doi.org/10.1016/S0300-483X\(99\)00020-7](https://doi.org/10.1016/S0300-483X(99)00020-7)
- Hoover, B.R., M.N. Reed, J. Su, R.D. Penrod, L.A. Kotilinek, M.K. Grant, R. Pistick, G.A. Carlson, L.M. Lanier, L.L. Yuan, et al. 2010. Tau mislocalization to dendritic spines mediates synaptic dysfunction independently of neurodegeneration. *Neuron*. 68:1067–1081. <https://doi.org/10.1016/j.neuron.2010.11.030>
- Howells, C., A.K. West, and R.S. Chung. 2010. Neuronal growth-inhibitory factor (metallothionein-3): Evaluation of the biological function of growth-inhibitory factor in the injured and neurodegenerative brain. *FEBS J.* 277:2931–2939. <https://doi.org/10.1111/j.1742-4658.2010.07718.x>

- Hu, H., M. Bandell, M.J. Petrus, M.X. Zhu, and A. Patapoutian. 2009. Zinc activates damage-sensing TRPA1 ion channels. *Nat. Chem. Biol.* 5: 183–190. <https://doi.org/10.1038/nchembio.146>
- Hu, J.Y., D.L. Zhang, X.L. Liu, X.S. Li, X.Q. Cheng, J. Chen, H.N. Du, and Y. Liang. 2017. Pathological concentration of zinc dramatically accelerates abnormal aggregation of full-length human Tau and thereby significantly increases Tau toxicity in neuronal cells. *Biochim. Biophys. Acta Mol. Basis Dis.* 1863:414–427. <https://doi.org/10.1016/j.bbadis.2016.11.022>
- Huang, J., A.J. Roberts, A.E. Leschziner, and S.L. Reck-Peterson. 2012. Lis1 acts as a “clutch” between the ATPase and microtubule-binding domains of the dynein motor. *Cell.* 150:975–986. <https://doi.org/10.1016/j.cell.2012.07.022>
- Huang, Y., Z. Wu, Y. Cao, M. Lang, B. Lu, and B. Zhou. 2014. Zinc binding directly regulates tau toxicity independent of tau hyperphosphorylation. *Cell Rep.* 8:831–842. <https://doi.org/10.1016/j.celrep.2014.06.047>
- Jakobs, M.A.H., A. Dimitracopoulos, and K. Franze. 2019. KymoButler, a deep learning software for automated kymograph analysis. *Elife.* 8:e42288. <https://doi.org/10.7554/eLife.42288>
- Janke, C., and J.C. Bulinski. 2011. Post-translational regulation of the microtubule cytoskeleton: Mechanisms and functions. *Nat. Rev. Mol. Cell Biol.* 12:773–786. <https://doi.org/10.1038/nrm3227>
- Janke, C., and M.M. Magiera. 2020. The tubulin code and its role in controlling microtubule properties and functions. *Nat. Rev. Mol. Cell Biol.* 21: 307–326. <https://doi.org/10.1038/s41580-020-0214-3>
- Johnson, K.A. 1983. The pathway of ATP hydrolysis by dynein. Kinetics of a presteady state phosphate burst. *J. Biol. Chem.* 258:13825–13832. [https://doi.org/10.1016/S0021-9258\(17\)43992-5](https://doi.org/10.1016/S0021-9258(17)43992-5)
- Kang, J.S., J.H. Tian, P.Y. Pan, P. Zald, C. Li, C. Deng, and Z.H. Sheng. 2008. Docking of axonal mitochondria by syntaphilin controls their mobility and affects short-term facilitation. *Cell.* 132:137–148. <https://doi.org/10.1016/j.cell.2007.11.024>
- Kapitein, L.C., M.A. Schlager, W.A. van der Zwan, P.S. Wulf, N. Keijzer, and C.C. Hoogenraad. 2010. Probing intracellular motor protein activity using an inducible cargo trafficking assay. *Biophys. J.* 99:2143–2152. <https://doi.org/10.1016/j.bpj.2010.07.055>
- Kardon, J.R., and R.D. Vale. 2009. Regulators of the cytoplasmic dynein motor. *Nat. Rev. Mol. Cell Biol.* 10:854–865. <https://doi.org/10.1038/nrm2804>
- Kellogg, E.H., N.M.A. Hejab, S. Poepsel, K.H. Downing, F. DiMaio, and E. Nogales. 2018. Near-atomic model of microtubule-tau interactions. *Science.* 360:1242–1246. <https://doi.org/10.1126/science.aat1780>
- Koh, J.Y., S.W. Suh, B.J. Gwag, Y.Y. He, C.Y. Hsu, and D.W. Choi. 1996. The role of zinc in selective neuronal death after transient global cerebral ischemia. *Science.* 272:1013–1016. <https://doi.org/10.1126/science.272.5264.1013>
- Kosik, K.S., and E.A. Finch. 1987. MAP2 and tau segregate into dendritic and axonal domains after the elaboration of morphologically distinct neurites: An immunocytochemical study of cultured rat cerebrum. *J. Neurosci.* 7: 3142–3153. <https://doi.org/10.1523/JNEUROSCI.07-10-03142.1987>
- Lacey, S.E., S. He, S.H. Scheres, and A.P. Carter. 2019. Cryo-EM of dynein microtubule-binding domains shows how an axonemal dynein distorts the microtubule. *Elife.* 8:e47145. <https://doi.org/10.7554/eLife.47145>
- Lasser, M., J. Tiber, and L.A. Lowery. 2018. The role of the microtubule cytoskeleton in neurodevelopmental disorders. *Front. Cell. Neurosci.* 12: 165. <https://doi.org/10.3389/fncel.2018.00165>
- Lin, Y.F., C.W. Cheng, C.S. Shih, J.K. Hwang, C.S. Yu, and C.H. Lu. 2016. MIB: Metal ion-binding site prediction and docking server. *J. Chem. Inf. Model.* 56:2287–2291. <https://doi.org/10.1021/acs.jcim.6b00407>
- Maday, S., A.E. Twelvetrees, A.J. Moughamian, and E.L. Holzbaur. 2014. Axonal transport: Cargo-specific mechanisms of motility and regulation. *Neuron.* 84:292–309. <https://doi.org/10.1016/j.neuron.2014.10.019>
- Magiera, M.M., S. Bodakuntla, J. Ziak, S. Lacomme, P. Marques Sousa, S. Leboucher, T.J. Hausrat, C. Bosc, A. Andrieux, M. Kneussel, et al. 2018. Excessive tubulin polyglutamylation causes neurodegeneration and perturbs neuronal transport. *EMBO J.* 37:e100440. <https://doi.org/10.15252/embj.2018100440>
- Mahamdeh, M., S. Simmert, A. Luchniak, E. Schäffer, and J. Howard. 2018. Label-free high-speed wide-field imaging of single microtubules using interference reflection microscopy. *J. Microsc.* 272:60–66. <https://doi.org/10.1111/jmi.12744>
- Malaiyandi, L.M., A.S. Honick, G.L. Rintoul, Q.J. Wang, and I.J. Reynolds. 2005. Zn²⁺ inhibits mitochondrial movement in neurons by phosphatidylinositol 3-kinase activation. *J. Neurosci.* 25:9507–9514. <https://doi.org/10.1523/JNEUROSCI.0868-05.2005>
- Manka, S.W., and C.A. Moores. 2018. The role of tubulin-tubulin lattice contacts in the mechanism of microtubule dynamic instability. *Nat. Struct. Mol. Biol.* 25:607–615. <https://doi.org/10.1038/s41594-018-0087-8>
- Manka, S.W., and C.A. Moores. 2020. Pseudo-repeats in doublecortin make distinct mechanistic contributions to microtubule regulation. *EMBO Rep.* 21:e51534. <https://doi.org/10.15252/embr.202051534>
- Maret, W. 2017. Zinc in cellular regulation: The nature and significance of “zinc signals”. *Int. J. Mol. Sci.* 18:2285. <https://doi.org/10.3390/ijms18122285>
- Markus, S.M., M.G. Marzo, and R.J. McKenney. 2020. New insights into the mechanism of dynein motor regulation by lissencephaly-1. *Elife.* 9: e59737. <https://doi.org/10.7554/eLife.59737>
- Marzo, M.G., J.M. Griswold, and S.M. Markus. 2020. Pac1/LIS1 stabilizes an uninhibited conformation of dynein to coordinate its localization and activity. *Nat. Cell Biol.* 22:559–569. <https://doi.org/10.1038/s41556-020-0492-1>
- Meixner, A., S. Haverkamp, H. Wässle, S. Führer, J. Thalhammer, N. Kropf, R.E. Bittner, H. Lassmann, G. Wiche, and F. Propst. 2000. MAP1B is required for axon guidance and is involved in the development of the central and peripheral nervous system. *J. Cell Biol.* 151:1169–1178. <https://doi.org/10.1083/jcb.151.6.1169>
- Metzger, T., V. Gache, M. Xu, B. Cadot, E.S. Folker, B.E. Richardson, E.R. Gomes, and M.K. Baylies. 2012. MAP and kinesin-dependent nuclear positioning is required for skeletal muscle function. *Nature.* 484: 120–124. <https://doi.org/10.1038/nature10914>
- Minckley, T.F., C. Zhang, D.H. Fudge, A.M. Dischler, K.D. Lejeune, H. Xu, and Y. Qin. 2019. Sub-nanomolar sensitive GZnP3 reveals TRPML1-mediated neuronal Zn²⁺ signals. *Nat. Commun.* 10:4806. <https://doi.org/10.1038/s41467-019-12761-x>
- Monroy, B.Y., D.L. Sawyer, B.E. Ackermann, M.M. Borden, T.C. Tan, and K.M. Ori-Mckenney. 2018. Competition between microtubule-associated proteins directs motor transport. *Nat. Commun.* 9:1487. <https://doi.org/10.1038/s41467-018-03909-2>
- Monroy, B.Y., T.C. Tan, J.M. Oclaman, J.S. Han, S. Simó, S. Niwa, D.W. Nowakowski, R.J. McKenney, and K.M. Ori-Mckenney. 2020. A combinatorial MAP code dictates polarized microtubule transport. *Dev. Cell.* 53:60–72.e4. <https://doi.org/10.1016/j.devcel.2020.01.029>
- Montagnac, G., V. Meas-Yedid, M. Irondele, A. Castro-Castro, M. Franco, T. Shida, M.V. Nachury, A. Benmerah, J.C. Olivo-Marin, and P. Chavrier. 2013. α TAT1 catalyses microtubule acetylation at clathrin-coated pits. *Nature.* 502:567–570. <https://doi.org/10.1038/nature12571>
- Moreira, G.G., J.S. Cristóvão, V.M. Torres, A.P. Carapeto, M.S. Rodrigues, I. Landrieu, C. Cordeiro, and C.M. Gomes. 2019. Zinc binding to tau influences aggregation kinetics and oligomer distribution. *Int. J. Mol. Sci.* 20:5979. <https://doi.org/10.3390/ijms20235979>
- Morfini, G.A., M. Burns, L.I. Binder, N.M. Kanaan, N. LaPointe, D.A. Bosco, R.H. Brown Jr, H. Brown, A. Tiwari, L. Hayward, et al. 2009. Axonal transport defects in neurodegenerative diseases. *J. Neurosci.* 29: 12776–12786. <https://doi.org/10.1523/JNEUROSCI.3463-09.2009>
- Nakashima, A.S., and R.H. Dyck. 2009. Zinc and cortical plasticity. *Brain Res. Brain Res. Rev.* 59:347–373. <https://doi.org/10.1016/j.brainresrev.2008.10.003>
- Nassal, J.P., F.H. Murphy, R.F. Toonen, and M. Verhage. 2022. Differential axonal trafficking of Neuropeptide Y-, LAMP1-, and RAB7-tagged organelles in vivo. *Elife.* 11:e81721. <https://doi.org/10.7554/eLife.81721>
- Niekamp, S., N. Coudray, N. Zhang, R.D. Vale, and G. Bhabha. 2019. Coupling of ATPase activity, microtubule binding, and mechanics in the dynein motor domain. *EMBO J.* 38:e101414. <https://doi.org/10.15252/emboj.2018101414>
- Palmiter, R.D., T.B. Cole, C.J. Quaife, and S.D. Findley. 1996. ZnT-3, a putative transporter of zinc into synaptic vesicles. *Proc. Natl. Acad. Sci. USA.* 93: 14934–14939. <https://doi.org/10.1073/pnas.93.25.14934>
- Petersen, E.F., T.D. Goddard, C.C. Huang, G.S. Couch, D.M. Greenblatt, E.C. Meng, and T.E. Ferrin. 2004. UCSF Chimera: A visualization system for exploratory research and analysis. *J. Comput. Chem.* 25:1605–1612. <https://doi.org/10.1002/jcc.20084>
- Planchon, T.A., L. Gao, D.E. Milkie, M.W. Davidson, J.A. Galbraith, C.G. Galbraith, and E. Betzig. 2011. Rapid three-dimensional isotropic imaging of living cells using Bessel beam plane illumination. *Nat. Methods.* 8: 417–423. <https://doi.org/10.1038/nmeth.1586>
- Porter, N.J., and D.W. Christianson. 2019. Structure, mechanism, and inhibition of the zinc-dependent histone deacetylases. *Curr. Opin. Struct. Biol.* 59:9–18. <https://doi.org/10.1016/j.sbi.2019.01.004>
- Pratt, E.P.S., L.J. Damon, K.J. Anson, and A.E. Palmer. 2021. Tools and techniques for illuminating the cell biology of zinc. *Biochim. Biophys. Acta Mol. Cell Res.* 1868:118865. <https://doi.org/10.1016/j.bbamcr.2020.118865>

- Qin, Y., P.J. Dittmer, J.G. Park, K.B. Jansen, and A.E. Palmer. 2011. Measuring steady-state and dynamic endoplasmic reticulum and Golgi Zn²⁺ with genetically encoded sensors. *Proc. Natl. Acad. Sci. USA*. 108:7351–7356. <https://doi.org/10.1073/pnas.1015686108>
- Reck-Peterson, S.L., A. Yildiz, A.P. Carter, A. Gennerich, N. Zhang, and R.D. Vale. 2006. Single-molecule analysis of dynein processivity and stepping behavior. *Cell*. 126:335–348. <https://doi.org/10.1016/j.cell.2006.05.046>
- Reed, N.A., D. Cai, T.L. Blasius, G.T. Jih, E. Meyhofer, J. Gaertig, and K.J. Verhey. 2006. Microtubule acetylation promotes kinesin-1 binding and transport. *Curr. Biol.* 16:2166–2172. <https://doi.org/10.1016/j.cub.2006.09.014>
- Religa, D., D. Strozzyk, R.A. Cherny, I. Volitakis, V. Haroutunian, B. Winblad, J. Naslund, and A.I. Bush. 2006. Elevated cortical zinc in Alzheimer disease. *Neurology*. 67:69–75. <https://doi.org/10.1212/01.wnl.0000223644.08653.b5>
- Rogowski, K., J. van Dijk, M.M. Magiera, C. Bosc, J.C. Deloulme, A. Bosson, L. Peris, N.D. Gold, B. Lacroix, M. Bosch Grau, et al. 2010. A family of protein-deglutamylation enzymes associated with neurodegeneration. *Cell*. 143:564–578. <https://doi.org/10.1016/j.cell.2010.10.014>
- Salentin, S., S. Schreiber, V.J. Haupt, M.F. Adamse, and M. Schroeder. 2015. PLIP: Fully automated protein-ligand interaction profiler. *Nucleic Acids Res.* 43:W443–W447. <https://doi.org/10.1093/nar/gkv315>
- Sanford, L., and A.E. Palmer. 2020. Dissociated hippocampal neurons exhibit distinct Zn²⁺ dynamics in a stimulation-method-dependent manner. *ACS Chem. Neurosci.* 11:508–514. <https://doi.org/10.1021/acschemneuro.0c00006>
- Sanford, L., M.C. Carpenter, and A.E. Palmer. 2019. Intracellular Zn²⁺ transients modulate global gene expression in dissociated rat hippocampal neurons. *Sci. Rep.* 9:9411. <https://doi.org/10.1038/s41598-019-45844-2>
- Scales, T.M., S. Lin, M. Kraus, R.G. Goold, and P.R. Gordon-Weeks. 2009. Nonprimed and DYRK1A-primed GSK3 beta-phosphorylation sites on MAP1B regulate microtubule dynamics in growing axons. *J. Cell Sci.* 122:2424–2435. <https://doi.org/10.1242/jcs.040162>
- Schimert, K.I., B.G. Budaitis, D.N. Reinemann, M.J. Lang, and K.J. Verhey. 2019. Intracellular cargo transport by single-headed kinesin motors. *Proc. Natl. Acad. Sci. USA*. 116:6152–6161. <https://doi.org/10.1073/pnas.1817924116>
- Schindelin, J., I. Arganda-Carreras, E. Frise, V. Kaynig, M. Longair, T. Pietzsch, S. Preibisch, C. Rueden, S. Saalfeld, B. Schmid, et al. 2012. Fiji: An open-source platform for biological-image analysis. *Nat. Methods*. 9:676–682. <https://doi.org/10.1038/nmeth.2019>
- Sensi, S.L., P. Paoletti, A.I. Bush, and I. Sekler. 2009. Zinc in the physiology and pathology of the CNS. *Nat. Rev. Neurosci.* 10:780–791. <https://doi.org/10.1038/nrn2734>
- Shang, Z., K. Zhou, C. Xu, R. Csencsits, J.C. Cochran, and C.V. Sindelar. 2014. High-resolution structures of kinesin on microtubules provide a basis for nucleotide-gated force-generation. *Elife*. 3:e04686. <https://doi.org/10.7554/eLife.04686>
- Sherer, N.M., M.J. Lehmann, L.F. Jimenez-Soto, A. Ingmundson, S.M. Horner, G. Cicchetti, P.G. Allen, M. Pypaert, J.M. Cunningham, and W. Mothes. 2003. Visualization of retroviral replication in living cells reveals budding into multivesicular bodies. *Traffic*. 4:785–801. <https://doi.org/10.1034/j.1600-0854.2003.00135.x>
- Shin, J.E., B.R. Miller, E. Babetto, Y. Cho, Y. Sasaki, S. Qayum, E.V. Russler, V. Cavalli, J. Milbrandt, and A. DiAntonio. 2012. SCG10 is a JNK target in the axonal degeneration pathway. *Proc. Natl. Acad. Sci. USA*. 109:E3696–E3705. <https://doi.org/10.1073/pnas.1216204109>
- Singh, V., L. Xu, S. Boyko, K. Surewicz, and W.K. Surewicz. 2020. Zinc promotes liquid-liquid phase separation of tau protein. *J. Biol. Chem.* 295:5850–5856. <https://doi.org/10.1074/jbc.AC120.013166>
- Sleigh, J.N., A.M. Rossor, A.D. Fellows, A.P. Tosolini, and G. Schiavo. 2019. Axonal transport and neurological disease. *Nat. Rev. Neurol.* 15:691–703. <https://doi.org/10.1038/s41582-019-0257-2>
- Tan, R., A.J. Lam, T. Tan, J. Han, D.W. Nowakowski, M. Vershinin, S. Simó, K.M. Ori-McKenney, and R.J. McKenney. 2019. Microtubules gate tau condensation to spatially regulate microtubule functions. *Nat. Cell Biol.* 21:1078–1085. <https://doi.org/10.1038/s41556-019-0375-5>
- Tanaka, T., F.F. Serneo, C. Higgins, M.J. Gambello, A. Wynshaw-Boris, and J.G. Gleeson. 2004. Lis1 and doublecortin function with dynein to mediate coupling of the nucleus to the centrosome in neuronal migration. *J. Cell Biol.* 165:709–721. <https://doi.org/10.1083/jcb.200309025>
- Tantama, M., J.R. Martínez-François, R. Mongeon, and G. Yellen. 2013. Imaging energy status in live cells with a fluorescent biosensor of the intracellular ATP-to-ADP ratio. *Nat. Commun.* 4:2550. <https://doi.org/10.1038/ncomms3550>
- Lewis, T.L., Jr, G.F. Turi, S.K. Kwon, A. Losonczy, and F. Polleux. 2016. Progressive decrease of mitochondrial motility during maturation of cortical axons In Vitro and In Vivo. *Curr. Biol.* 26:2602–2608. <https://doi.org/10.1016/j.cub.2016.07.064>
- Tymanskyj, S.R., B. Yang, A. Fahnkar, A.C. Lepore, and L. Ma. 2017. MAP7 regulates axon collateral branch development in dorsal root ganglion neurons. *J. Neurosci.* 37:1648–1661. <https://doi.org/10.1523/JNEUROSCI.3260-16.2017>
- Tymanskyj, S.R., B.H. Yang, K.J. Verhey, and L. Ma. 2018. MAP7 regulates axon morphogenesis by recruiting kinesin-1 to microtubules and modulating organelle transport. *Elife*. 7:e36374. <https://doi.org/10.7554/eLife.36374>
- Uchimura, S., Y. Oguchi, Y. Hachikubo, S. Ishiwata, and E. Muto. 2010. Key residues on microtubule responsible for activation of kinesin ATPase. *EMBO J.* 29:1167–1175. <https://doi.org/10.1038/emboj.2010.25>
- Vershinin, M., J. Xu, D.S. Razafsky, S.J. King, and S.P. Gross. 2008. Tuning microtubule-based transport through filamentous MAPs: The problem of dynein. *Traffic*. 9:882–892. <https://doi.org/10.1111/j.1600-0854.2008.00741.x>
- Wang, X., and T.L. Schwarz. 2009. The mechanism of Ca²⁺-dependent regulation of kinesin-mediated mitochondrial motility. *Cell*. 136:163–174. <https://doi.org/10.1016/j.cell.2008.11.046>
- Wang, Y., I. Lorenzi, O. Georgiev, and W. Schaffner. 2004. Metal-responsive transcription factor-1 (MTF-1) selects different types of metal response elements at low vs. high zinc concentration. *Biol. Chem.* 385:623–632. <https://doi.org/10.1515/BC.2004.077>
- Watson, P., and D.J. Stephens. 2006. Microtubule plus-end loading of p150(Glued) is mediated by EB1 and CLIP-170 but is not required for intracellular membrane traffic in mammalian cells. *J. Cell Sci.* 119:2758–2767. <https://doi.org/10.1242/jcs.02999>
- Wolf, S.G., G. Mosser, and K.H. Downing. 1993. Tubulin conformation in zinc-induced sheets and microtubules. *J. Struct. Biol.* 111:190–199. <https://doi.org/10.1006/jsbi.1993.1049>
- Yang, M., M. Wu, P. Xia, C. Wang, P. Yan, Q. Gao, J. Liu, H. Wang, X. Duan, and X. Yang. 2012. The role of microtubule-associated protein 1B in axonal growth and neuronal migration in the central nervous system. *Neural Regen. Res.* 7:842–848. <https://doi.org/10.3969/j.issn.1673-5374.2012.11.008>
- Yi, M., D. Weaver, and G. Hajnóczky. 2004. Control of mitochondrial motility and distribution by the calcium signal: A homeostatic circuit. *J. Cell Biol.* 167:661–672. <https://doi.org/10.1083/jcb.200406038>
- Zhang, Y., N. Li, C. Caron, G. Matthias, D. Hess, S. Khochbin, and P. Matthias. 2003. HDAC-6 interacts with and deacetylates tubulin and microtubules in vivo. *EMBO J.* 22:1168–1179. <https://doi.org/10.1093/emboj/cdg115>
- Zhang, C., D. Maslar, T.F. Minckley, K.D. Lejeune, and Y. Qin. 2021. Spontaneous, synchronous zinc spikes oscillate with neural excitability and calcium spikes in primary hippocampal neuron culture. *J. Neurochem.* 157:1838–1849. <https://doi.org/10.1111/jnc.15334>
- Zyśk, M., B. Gapys, A. Ronowska, S. Gul-Hinc, A. Erlandsson, A. Iwanicki, M. Sakowicz-Burkiewicz, A. Szutowicz, and H. Bielarczyk. 2018. Protective effects of voltage-gated calcium channel antagonists against zinc toxicity in SN56 neuroblastoma cholinergic cells. *PLoS One*. 13:e0209363. <https://doi.org/10.1371/journal.pone.0209363>

Supplemental material

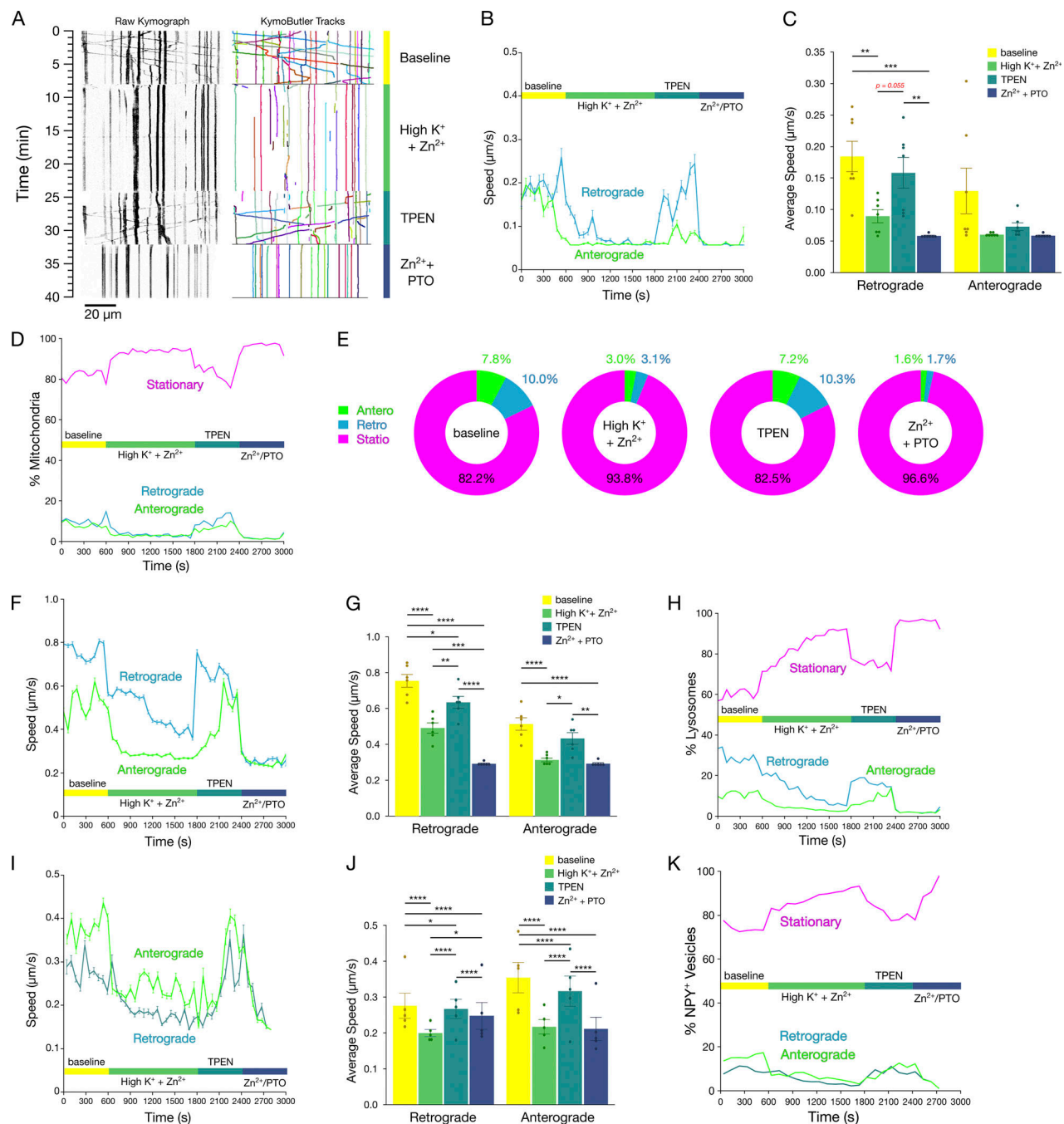


Figure S1. **Zn²⁺ influx arrests axonal transport of mitochondria, lysosomes, and NPY⁺ vesicles.** (A) Representative kymographs (left) and measured tracks (identified using KymoButler; right) of mito-mCherry motility along axons from primary cultured rat hippocampal neurons prior to ("baseline"; top) or after initiation of Zn²⁺ influx by high K⁺ depolarization (middle-top), following washout and addition of 100 μM TPEN (middle-bottom), and then washout and addition of 100 μM Zn²⁺ and 2.5 μM PTO (bottom). (B) Mean instantaneous speed (±SEM) of mitochondria moving retrograde (blue) or anterograde (green) across baseline, Zn²⁺ influx by high K⁺ depolarization, TPEN, and Zn²⁺ + PTO treatment (60-s binned, representing 7 axons). (C) Mean speed (±SEM) of mitochondria moving in the indicated directions for each condition (n = 7 axons from three independent replicates). (D) Proportions of mitochondria moving in the indicated directions across baseline, depolarization with Zn²⁺, TPEN, and Zn²⁺ + PTO treatment (60-s binned, representing 7 axons). (E) Mean proportions of mitochondrial motility for each condition. (F) Mean instantaneous speed (±SEM) of lysosomes moving retrograde (blue) or anterograde (green) across baseline, Zn²⁺ influx by high K⁺ depolarization, following washout and addition of 100 μM TPEN, and then washout and addition of 100 μM Zn²⁺ and 2.5 μM PTO (bottom; 60-s binned, representing 6 axons). (G) Mean speed (±SEM) of lysosomes moving in the indicated directions for each condition (n = 6 axons from three independent replicates). (H) Proportions of lysosomes moving in the indicated directions across baseline, Zn²⁺ influx by high K⁺ depolarization, TPEN, and Zn²⁺ + PTO treatment (60-s binned, representing 6 axons). (I) Mean instantaneous speed (±SEM) of NPY⁺ vesicles moving retrograde (blue) or anterograde (green) across baseline, 100 μM Zn²⁺ and 2.5 μM PTO, and addition of 100 μM TPEN after washout (30-s binned, representing 5 axons). (J) Mean speed of NPY⁺ vesicles moving in the indicated directions for each condition (n = 5 axons from five independent replicates). (K) Proportions of NPY⁺ vesicles moving in the indicated directions across baseline, depolarization with Zn²⁺, TPEN, and Zn²⁺ + PTO treatment (30-s binned, representing 5 axons). All experiments were performed in the absence of extracellular Ca²⁺. **** P < 0.0001, *** P < 0.001, ** P < 0.01, * P < 0.05, n.s. not significant.

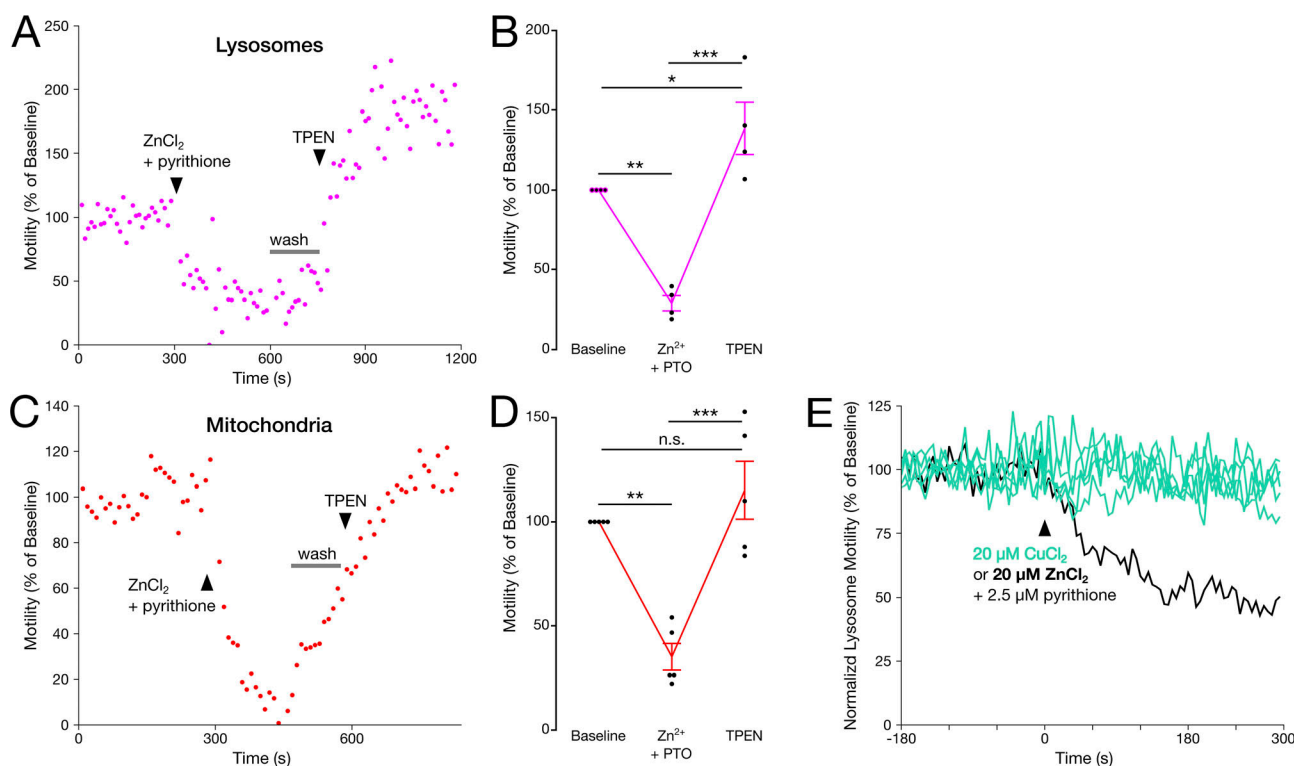


Figure S2. Zn^{2+} influx inhibits motility of lysosomes and mitochondria in HeLa cells. (A and C) Representative lysosomal (A) and mitochondrial (C) motility (determined using the Total Motility plugin for Fiji; see Materials and methods) in HeLa cells treated with $20\ \mu\text{M}$ ZnCl_2 and $1.25\ \mu\text{M}$ pyrithione (PTO), then washed and treated with $100\ \mu\text{M}$ TPEN (treatments added at time points indicated on plots). (B and D) Mean (\pm SEM) lysosomal (B) and mitochondrial (D) motility normalized to their respective baselines ($n = 4$ and 5 cells, from four to three independent replicates, respectively). One-way repeated measures ANOVA, with post-hoc Tukey HSD. (E) Representative traces of lysosomal motility in HeLa cells stained with LysoTracker Red and treated with $2.5\ \mu\text{M}$ pyrithione and either $20\ \mu\text{M}$ CuCl_2 (teal lines) or $20\ \mu\text{M}$ ZnCl_2 (black line) at 0 sec. All experiments were performed in the absence of extracellular Ca^{2+} . *** $P < 0.0001$, ** $P < 0.01$, * $P < 0.05$, n.s. not significant.

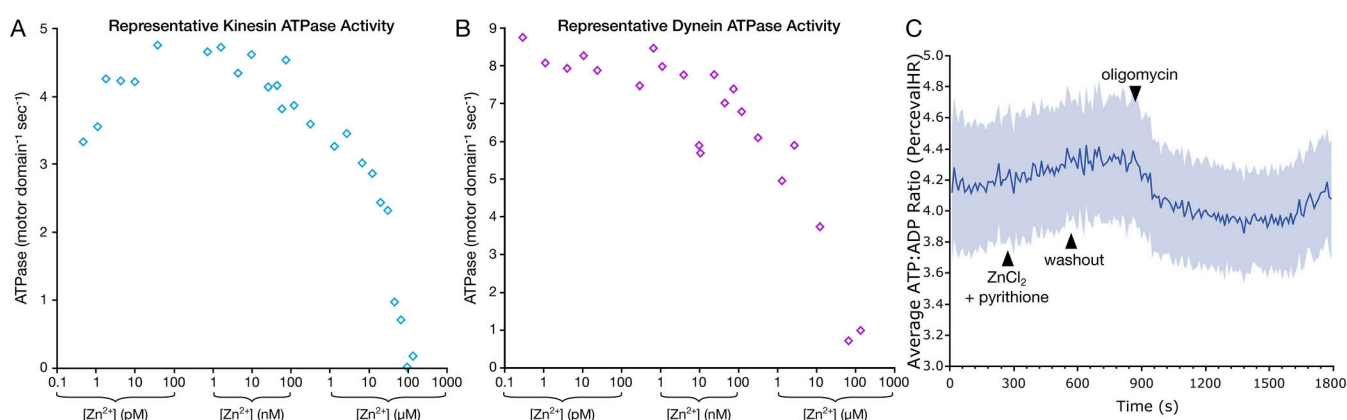


Figure S3. Supplemental in vitro analysis of the effect of Zn^{2+} on kinesin and dynein motor activity, and in situ investigation of ATP/ADP levels in COS-7 cells. (A and B) Representative microtubule-stimulated ATPase activity showing non-normalized ATPase activity per motor domain per second for purified (A) recombinant human kinesin (KIF5A) or (B) a minimally processive, artificially dimerized yeast dynein fragment (GST-dynein₃₃₁) across a range of Zn^{2+} concentrations (from same dataset as Fig. 5, A and B). (C) Mean ATP:ADP ratio (\pm SEM) in COS-7 cells as measured by PercevalHR across baseline, $100\ \mu\text{M}$ ZnCl_2 and $2.5\ \mu\text{M}$ pyrithione, washout, and 2.5 – $5\ \mu\text{M}$ oligomycin treatment (representing seven cells from three individual replicates).

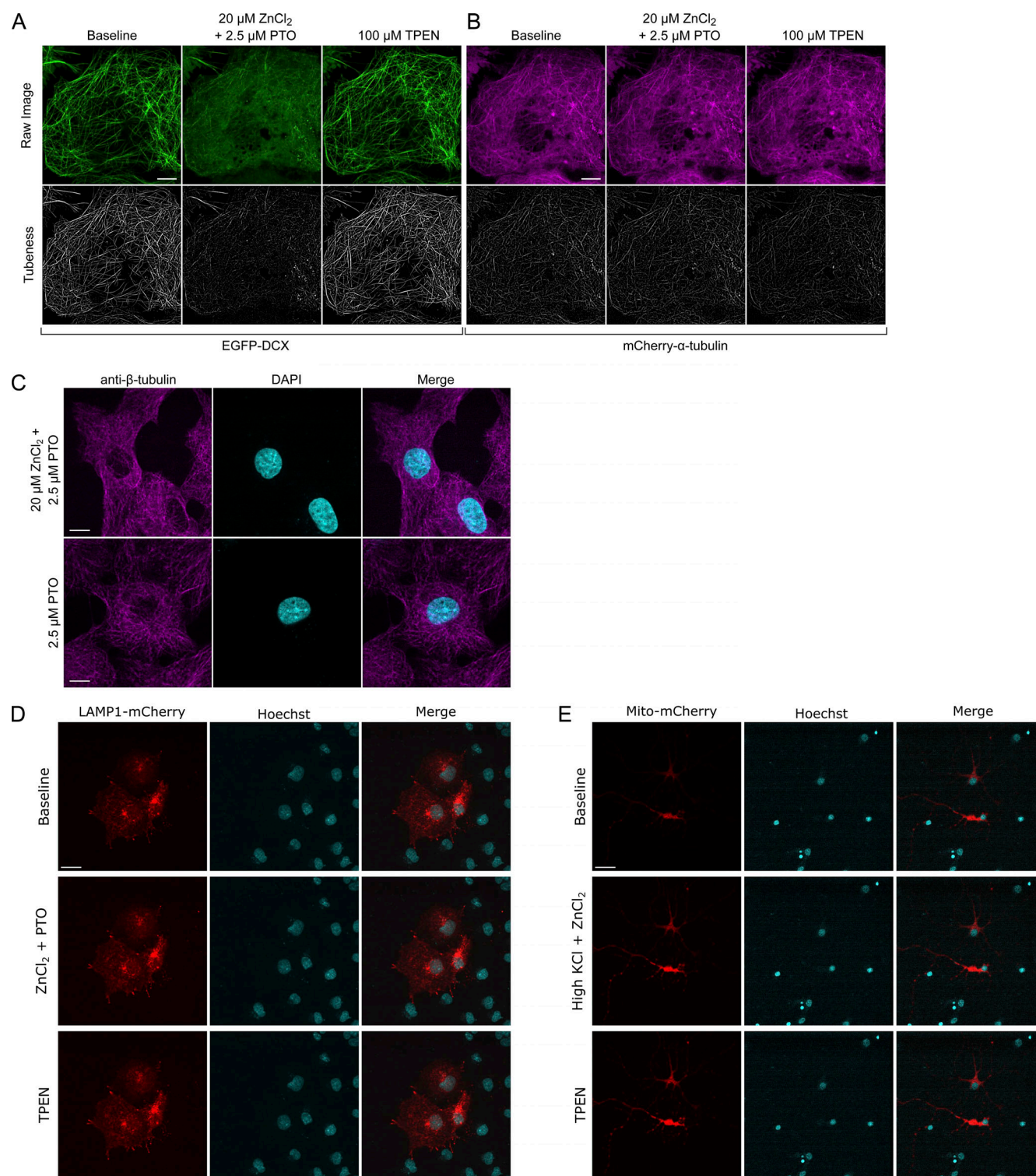


Figure S4. Tubeness analysis, endogenous tubulin controls, and nuclear health controls. (A and B) Representative micrographs of COS-7 cells expressing (A) EGFP-DCX and (B) mCherry-α-tubulin before treatment ("baseline," left), after 5-min treatment with 20 μM ZnCl₂ and 2.5 μM PTO (center), or after subsequent treatment with 100 μM TPEN (right). Scale bar = 10 μm. Raw fluorescence images (top) and "Tubeness" analysis (Fiji Plugin; bottom) are shown. (C) Representative micrographs of methanol-fixed COS-7 cells treated with 2 μM pyrithione in the presence (top) or absence (bottom) of 20 μM ZnCl₂. Fixed cells were incubated with anti-β-tubulin monoclonal antibodies (magenta, left), DAPI (cyan, center), and channels are shown merged (right). Scale bar = 10 μm. (D) Representative micrographs of COS-7 cells expressing LAMP1-mCherry (left), stained with Hoechst (middle), and merged images (right) before treatment ("baseline," top), after 5-min treatment with 20 μM ZnCl₂ and 2.5 μM PTO (middle), or after subsequent treatment with 100 μM TPEN (bottom). Scale bar = 30 μm. (E) Representative micrographs of primary hippocampal neurons expressing mito-mCherry (left) and stained with Hoechst (middle) and merged images (right) before treatment ("baseline," top), after 5-min Zn²⁺ influx by high K⁺ depolarization (middle), or after subsequent treatment with 100 μM TPEN (bottom). Scale bar = 30 μm. All experiments were performed in the absence of extracellular Ca²⁺.

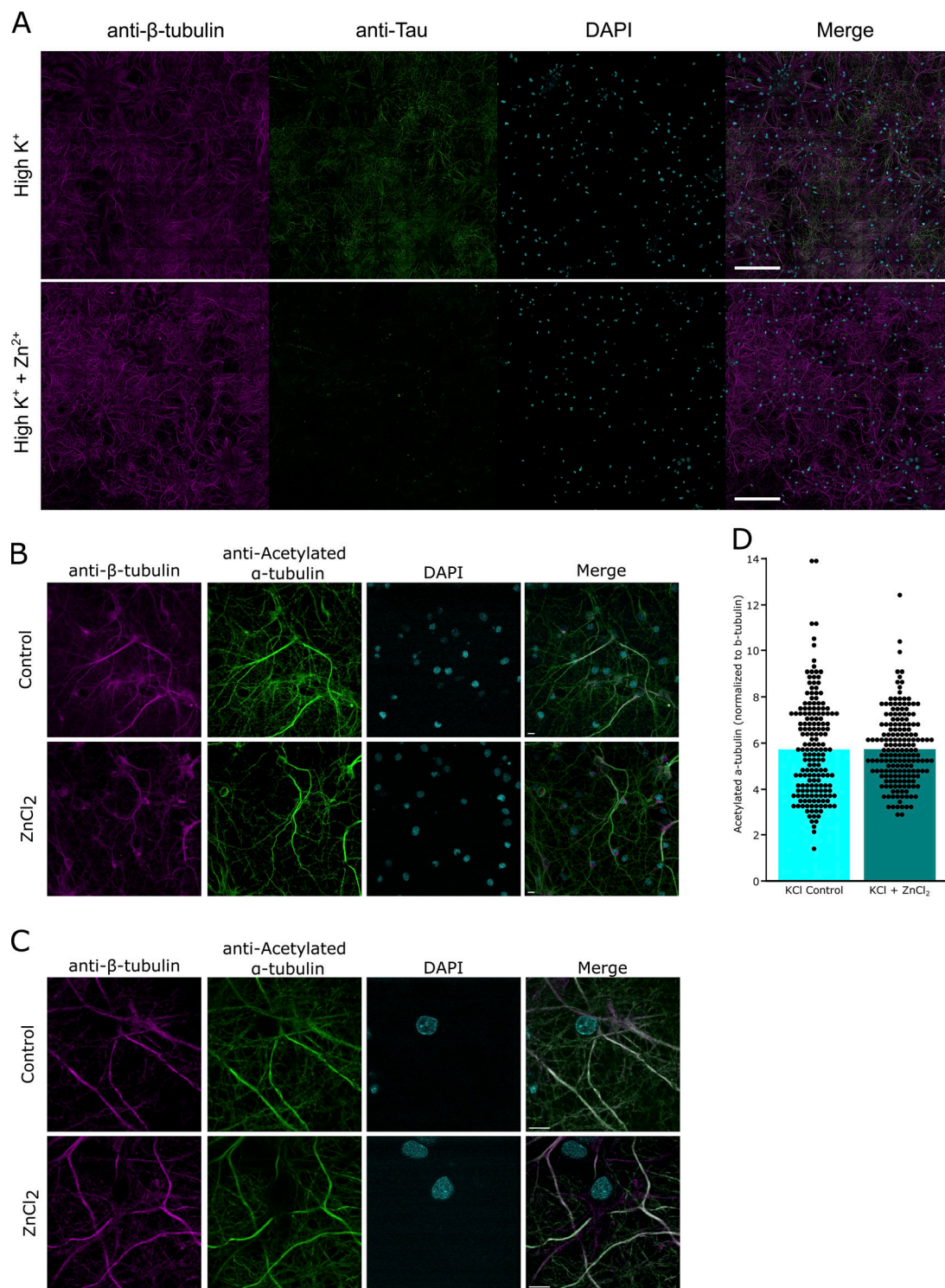


Figure S5. Zn^{2+} influx promotes detachment of endogenous neuronal Tau but no changes in microtubule acetylation in situ. (A) Representative immunofluorescence micrographs (15×15 stitched image grid, 5% overlap) of methanol-fixed primary rat hippocampal neurons depolarized with 50 mM KCl in the absence (top) or presence (bottom) of 100 μM $ZnCl_2$. Fixed cells were incubated with anti- β -tubulin monoclonal antibodies (magenta, left), anti-Tau polyclonal antibodies (green, left center), DAPI (cyan, right center), and channels are shown merged (right). Scale bar = 200 μm . (B and C) Representative immunofluorescence micrographs at (B) low magnification or (C) high magnification, of methanol-fixed primary rat hippocampal neurons depolarized with 50 mM KCl in the absence (top) or presence (bottom) of 100 μM $ZnCl_2$. Fixed cells were incubated with anti- β -tubulin monoclonal antibodies (magenta, left), anti-acetylated α -tubulin polyclonal antibodies (green, left center), DAPI (cyan, right center), and channels are shown merged (right). Scale bar = 10 μm . (D) Mean fluorescence intensity of AlexaFluor 488 secondary antibody-labeled acetylated α -tubulin (normalized to AlexaFluor 555-conjugated β -tubulin monoclonal antibodies) in neurons depolarized with 50 mM KCl in the absence or presence of 100 μM $ZnCl_2$ (50 mM KCl: $n = 180$ linear segments from three biological replicates; 50 mM KCl and 100 μM $ZnCl_2$: $n = 180$ linear segments from three biological replicates). All experiments were performed in the absence of extracellular Ca^{2+} .

Video 1. **Depolarization-induced influx of Zn^{2+} arrests axonal transport of lysosomes.** LAMP1-mCherry labeled lysosomes moving along axons of primary rat hippocampal neurons during baseline, depolarization induced Zn^{2+} influx (High K + Zn^{2+}), and washout followed by TPEN treatment. Related to Fig. 1.

Video 2. **Depolarization-induced influx of Ca^{2+} does not inhibit axonal transport of lysosomes.** LAMP1-mCherry labeled lysosomes moving along axons of primary rat hippocampal neurons during baseline, depolarization induced Ca^{2+} influx (High K + Ca^{2+}), and washout. Related to Fig. 1.

Video 3. **Zn^{2+} influx arrests axonal transport of mitochondria.** mito-mCherry labeled mitochondria moving along axons of primary rat hippocampal neurons during baseline, depolarization induced Zn^{2+} influx (High K + Zn^{2+}), washout followed by TPEN treatment, and washout followed by Zn^{2+} and pyrithione (PTO) treatment. Related to Fig. S1.

Video 4. **Zn^{2+} inhibits organellar motility with nanomolar IC_{50} in HeLa cells and neuronal axons.** Simultaneous imaging of Zn^{2+} (using GZnP2 sensor) and either lysosome (LAMP1-mCherry) or mitochondria (mito-mCherry) motility in HeLa cells (left and center panels) or neuronal axons (right panel). Related to Fig. 2 and Fig. S2.

Video 5. **Zn^{2+} inhibits KIF5A movement in situ in a dose-dependent manner.** Peroxisome dispersion assays in COS-7 cells expressing KIF5A(1-560)-mNG-FRB and PEX-mRFP-2xFKBP, during baseline, treatment with pyrithione (PTO) and varying concentrations of Zn^{2+} , and subsequent treatment with Zotarolimus. Related to Fig. 3.

Video 6. **Zn^{2+} redistributes KIF5A in COS-7 cells.** Distribution of KIF5A(1-560)-mNG-FRB and mCherry- α -tubulin in COS-7 cells during baseline and after Zn^{2+} and pyrithione (PTO) treatment. Related to Fig. S4.

Video 7. **Zn^{2+} promotes the dissociation of doublecortin from microtubules in situ.** Microtubule decoration of EGFP-DCX in COS-7 cells during baseline, Zn^{2+} and pyrithione (PTO) treatment, and Zn^{2+} chelation with 100 μ M TPEN. Related to Fig. 5.

Provided online are Table S1, Table S2, Table S3, and Table S4. Table S1 shows statistical analysis of ion effects on DCX decoration of microtubules. Table S2 shows statistical analysis of ion effects on Tau decoration of microtubules. Table S3 shows statistical analysis of ion effects on MAP2C decoration of microtubules. Table S4 shows statistical analysis of Zn^{2+} effect on MAP decoration of microtubules.